Hexose fluxes, mediated by vacuolar SWEET transporters, are important for xylem development in the inflorescence stem of *Arabidopsis thaliana*.

Emilie Aubry[1], Beate Hoffmann[1], Françoise Vilaine[1], Françoise Gilard[2], Patrick A.W. Klemens[3], Florence Guérard[2], Bertrand Gakière[2], H. Ekkehard Neuhaus[3], Catherine Bellini[1,4], Sylvie Dinant[1] and Rozenn Le Hir[1,*]

Affiliations

[1] Institut Jean-Pierre Bourgin, INRAE, AgroParisTech, Université Paris-Saclay, 78000 Versailles, France

[2] Plateforme Métabolisme-Métabolome, Institute of Plant Sciences Paris-Saclay IPS2, CNRS, INRAE, Univ Paris Sud, Univ Evry, Univ Paris-Diderot, Sorbonne Paris-Cité, Université Paris-Saclay, Bâtiment 360, Rue de Noetzlin, 91192 Gif sur Yvette, France

[3] Universität Kaiserslautern, Pflanzenphysiologie, Postfach 3049, D-67653 Kaiserslautern, Germany

[4] Umeå Plant Science Centre, Department of Plant Physiology, Umeå University, 90187 Umeå, Sweden

* Author for correspondence

Contact information:

Rozenn Le Hir

Telephone: +33 1 30 83 30 57

Fax: +33 1 30 83 30 96

Email : rozenn.le-hir@inrae.fr

ORCID ID: 0000-0001-6076-5863

Running title: Vacuolar hexose transport and xylem development

ABSTRACT

In higher plants, the development of the vascular system is controlled by a complex network of transcription factors. However, how nutrient availability in the vascular cells affects their development remains to be addressed. At the cellular level, cytosolic sugar availability is regulated mainly by sugar exchanges at the tonoplast through active and/or facilitated transport. In *Arabidopsis thaliana*, among the tonoplastic transporters, SWEET16 and SWEET17 have been previously localized in the vascular system. Here, using a reverse genetic approach, we propose that sugar exchanges at the tonoplast, mediated by SWEET16, are important for xylem cell division as revealed in particular by the decreased number of xylem cells in the *swt16* mutant and the expression of *SWEET16* at the procambium-xylem boundary. In addition, we demonstrate that transport of hexoses mediated by SWEET16 and/or SWEET17 is required to sustain the formation of the xylem secondary cell wall. This result is in line with a defect in the xylem cell wall composition as measured by FTIR in the *swt16swt17* double mutant and by upregulation of several genes involved in secondary cell wall synthesis. Our work therefore supports a model in which xylem development is partially dependent on the exchange of hexoses at the tonoplast of xylem-forming cells.

Keywords: Vacuole, tonoplast, sugar, transport, xylem, development, Arabidopsis, inflorescence stem

INTRODUCTION

The plant vasculature, composed of phloem, procambium/cambium, and xylem, is an elaborate system responsible for the transport of most biological compounds throughout the plant (Lucas et al., 2013). At the molecular level, vasculature development is governed by a complex network of transcription factors that are under the control of several signals, including hormones, peptides, and miRNAs (Fukuda and Ohashi-Ito, 2019; Smit et al., 2019). However, within this well-organized framework, a certain plasticity is required to adjust to cellular variations in terms of the availability of nutrients (i.e. sugars and amino acids).

Sugars, which represent the main source of energy, are required for metabolic activities, and they serve as a carbon reserve, and as intermediates for the synthesis of cell wall polysaccharides. Additionally, they have morphogenetic activity and act as primary messengers in signal transduction pathways (Sakr et al., 2018). It is therefore logical that modifications of sugar metabolism, transport or signaling can lead to multiple defects in plant growth and development (Eveland and Jackson, 2012). However, despite this central role, the role of sugar availability in the development of the vascular system in general and more specifically in heterotrophic tissues such as cambium and xylem is still elusive.

In these tissues, it has been suggested that lateral transport of sugars, coming from leakages from phloem sieve tubes, provides the sugars needed for vascular cell development (Minchin and McNaughton, 1987; Sibout et al., 2008; Spicer, 2014; Furze et al., 2018). Lateral transport is especially crucial for xylem secondary cell wall formation, since sugars are intermediate compounds in the synthesis of the cell wall polysaccharides which represent 80 % of the secondary cell wall (Marriott et al., 2016; Verbančič et al., 2018). The xylem tissue thus represents a strong sink for sugars that must be imported from surrounding tissues to serve as the source of carbon and energy. This is supported by the fact that perturbations in sugar transport at the plasma membrane of vascular cells, *via* SWEET or SUT transporters, affect the composition of the xylem secondary cell wall both in aspen and in Arabidopsis inflorescence stems (Mahboubi et al., 2013; Le Hir et al., 2015). Furthermore, in the Arabidopsis inflorescence stem, it has been suggested that movements of sucrose and/or hexoses towards the apoplast, mediated by SWEET11 and SWEET12, occur between the vascular parenchyma cells and the developing conducting cells to drive cell wall formation in a cell-specific manner (Dinant et al., 2019). Intercellular sugar availability seems, therefore, to play an important role in xylem development. However, the question remains open as to whether modification of sugar partitioning within the vasculature cells is also of importance.

The vacuole represents the main storage compartment for numerous primary and specialized metabolites including sugars (Martinoia, 2018). In tobacco leaves, up to 98% of hexoses are found in the vacuole (Heineke et al., 1994), whereas in Arabidopsis leaves, sucrose is mostly present in the cytosol and vacuoles contain half of the glucose and fructose (Weiszmann et al., 2018). Sugar exchanges between the vacuole and the cytosol are therefore required for dynamic adjustment of the quantity of sugar needed for metabolic and signaling pathways. In herbaceous and ligneous plants, few sugar transporters have been functionally characterized at the tonoplast (Hedrich et al., 2015), and localization in the cells of the vascular system has been shown only for *SUC4/SUT4*, *ESL1*, *SWEET16* and *SWEET17* (Yamada et al., 2010; Payyavula et al., 2011; Chardon et al., 2013; Klemens et al., 2013). In *Populus*, sugar export mediated by the tonoplastic sucrose symporter PttSUT4 is required for carbon partitioning between the source leaves and the lateral sinks (e.g. xylem). In Arabidopsis, we previously showed that the *SWEET16* promoter is active in the xylem parenchyma cells (Klemens et al., 2013), while the *SWEET17* promoter is active in the xylem parenchyma cells and young xylem cells of the Arabidopsis inflorescence stem (Chardon et al., 2013). Moreover high levels of *SWEET17* transcripts have been measured in the inflorescence stem, compared to other organs, after 7 to 8 weeks of growth (Guo et al., 2014). *SWEET16* and *SWEET17* are therefore good candidates with which to assess whether the maintenance of sugar homeostasis between the cytosol and the vacuole influences xylem development in Arabidopsis.

In the present work, through a reverse genetic approach, we demonstrate that SWEET16 and SWEET17 have specific and overlapping roles during xylem development. In particular, we suggest that sugar exchanges across the procambium-xylem boundary mediated by SWEET16 are important for xylem cell proliferation. By using infrared spectroscopy and gene expression analysis, we also show that both *SWEET16* and *SWEET17* are required for correct development of the secondary cell wall of xylem cells. Finally, since glucose and fructose accumulation are observed in the inflorescence stem of the double mutant, we suggest that maintenance of hexose homeostasis through the action of SWEET16 and/or SWEET17 is important at different stages of xylem development.

RESULTS

Radial growth of the inflorescence stem is altered in the *swt16swt17* double mutant

To explore to what extent mutations in *SWEET16* and/or *SWEET17* impact inflorescence stem development in Arabidopsis, we used the previously described *sweet17-1* (hereafter called *swt17*) mutant line (Chardon et al., 2013) and identified two new T-DNA insertion lines in the *SWEET16* gene. The mutants *sweet16-3* (SM_3.1827) and *sweet16-4* (SM_3.30075) possess an insertion in the promoter region and in the first exon of the *SWEET16* gene respectively (Supplemental Figure 1A). They were named after the previous alleles already published (Guo et al., 2014). A full-length *SWEET16* transcript was detected by RT-PCR in the *sweet16-3* allele, while no full-length transcript could be detected in the *sweet16-4* allele (Supplemental Figure 1B and 1C). The *sweet16-4* allele (hereafter called *swt16*) was therefore deemed to be a null allele. We generated the double mutant *sweet16sweet17* (hereafter called *swt16swt17*) and confirmed by RT-PCR that both genes full length were absent in this double mutant (Supplemental Figure 1C).

Analysis of the inflorescence stems of the *swt16*, *swt17* and *swt16swt17* mutants showed that the area of stem cross-sections was significantly smaller compared to that of the wild-type (Figure 1A and B). More precisely, the stem of all mutant lines contained less xylem tissue compared with the wild type, while only the stem of *swt16swt17* displayed significantly less phloem tissue (Figure 1C-D). Additionally, the proportion of xylem or phloem per stem was calculated (Figure 1E-F). While no change in the proportion of phloem was observed in the mutants compared to the wild type (Figure 1E), a significant reduction in the xylem proportion was observed in the double *swt16swt17* mutant (Figure 1F). Both *SWEET16* and *SWEET17* are therefore required for proper xylem development and hence for proper radial growth of the stem.

SWEET16 but not *SWEET17* is required for proliferation of xylem cells

The phenotype of the xylem tissue was further analyzed on an independent set of plants (Figure 2). We first checked the robustness of the inflorescence stem phenotype and confirmed that the *swt16* and *swt17* single mutants and the *swt16swt17* double mutant consistently displayed a significantly thinner inflorescence stem compared to the wild type (Figure 2A). In addition, we confirmed our previous results that showed a significantly shorter inflorescence stem in the *swt17* mutant compared to the wild-type (Figure 2B) (Chardon et al., 2013).

Interestingly, we did not observed any alteration in the inflorescence stem height in *swt16* or *swt16swt17* compared to the wild type (Figure 2B).

The xylem phenotype was then studied in more detail by counting the number of xylary fibers (cells with an area of between 5-150 µm²) and xylem vessels (cells with an area greater than 150 µm²) as well as measuring the individual cross-sectional areas within each vascular bundle (Figure 2C-I). In the vascular bundles of the *swt16* and *swt16swt17* mutants, but not *swt17*, the area occupied by the xylem tissue was significantly smaller than in the wild type (Figure 2C). These changes could result from modification of either cell size or cell number. While no changes in the size of the xylary fibers or the xylem vessels were observed in any of the genotypes analyzed (Figure 2D-E), the total number of xylem cells per vascular bundle was significantly reduced, by about 20%, in the single mutant *swt16* and the double mutant *swt16swt17* but not in *swt17* (Figure 2F). The numbers of xylary fibers and xylem vessels per vascular bundle were significantly reduced in the stem of the *swt16* single and *swt16swt17* double mutant but not in the *swt17* mutant (Figure 2G-H). The decreased number of xylary fibers was proportional to that of xylem vessels since the vessels-to-fibers ratio was the same in the wild type and the *swt16*, *swt17* and *swt16swt17* mutant lines (Figure 2I).

Overall, these results show that the single *swt16* mutant and the *swt16swt17* double mutant have the same phenotype (Figure 2 and Supplemental Table 1) and suggest that the expression of *SWEET16*, but not that of *SWEET17*, is required for correct division of xylem cells.

***SWEET16* and *SWEET17* are required for normal secondary cell wall composition and development in xylem cells**

To explore whether modifications in the vacuolar transport of sugars impact the formation of the xylem cell wall, we first exploited the transcriptomic dataset obtained from plants overexpressing a dexamethasone (DEX)-inducible version of the *VASCULAR RELATED NAC-DOMAIN PROTEIN 7* (*VND7*) gene, the master secondary wall-inducing transcription factor (Li et al., 2016). These plants allow the transcriptional and metabolic changes occurring during secondary cell wall formation to be studied. From the RNA-seq dataset, we extracted information related to the expression of the family of *SWEET* genes at different time points after induction of *VND7* expression (Supplemental Figure 2). Out of the 17 *SWEET* genes identified in Arabidopsis, 7 were differentially expressed during secondary cell wall formation

(Supplementary Figure 2). Most interestingly, the vacuolar *SWEET2* and *SWEET17* were significantly upregulated 3 hours after DEX induction while *SWEET16* expression was upregulated 12 hours after DEX induction (Supplementary Figure 2). In contrast, the expression of genes encoding the plasma membrane localized SWEET transporters (e.g. *SWEET1*, *SWEET3*, *SWEET11* and *SWEET12*) was significantly downregulated during secondary cell wall formation (Supplementary Figure 2). Additional analysis of the dataset showed that *SWEET2* and *SWEET17* were co-regulated with genes related to cell wall synthesis (*CESA*, *SND2*, *SDN3*, *MYB46*) as well as those encoding other sugar transporters localized at the tonoplast (*ESL1*) or at the plasma membrane (*STP1*, *STP13* and *PMT4*) (Supplementary Table 2). These results support the fact that sugar export from the vacuole to the cytosol is ongoing during secondary cell wall formation, most probably to provide sugars to be used as intermediates for cell wall formation.

To assess whether *SWEET16* and *SWEET17* are indeed functionally involved in xylem secondary cell wall formation, we performed a targeted gene expression analysis including genes that are known to be part of the transcriptional network involved in stem cell proliferation/organization (*PXY*, *WOX4*) (Etchells et al., 2013), xylem cell identity (*ATHB8*) (Smetana et al., 2019), and secondary cell wall biosynthesis in vessels/fibers (*CESA4*, *CESA7*, *CESA8*, *KNAT7, MYB4, MYB43, MYB46, MYB52*, *MYB54*, *MYB58*, *MYB63*, *MYB83*, *MYB103*, *NST1*, *VND6*, *VND7*, *SND1*/*NST3*, *SND3, VNI2* and *XND1*) (Hussey et al., 2013) (Figure 3A-I). When looking at the overall transcriptional profile of the wild type and the *swt16*, *swt17* and *swt16swt17* mutants, two clusters can be identified (Figure 3A). The first cluster contains the wild type, the *swt16* and *swt17* single mutants, whereas the second includes only the *swt16swt17* double mutant. Only a subset of genes shows significantly increased expression among the different genotypes, namely *SND3*, *MYB103*, *MYB4*, *VNI2*, *SND1*, *MYB83*, *MYB54* and *MYB46* (Figure 3A), though a tendency, albeit not significant, is observed for *MYB43* (P=0.053) and *KNAT7* (P=0.091) (Figure 3A). Interestingly, all these genes belong to the transcriptional network involved in secondary cell wall biosynthesis in xylem vessels and/or in xylary fibers (for review Hussey et al., 2013). A Student's *t*-test was then performed to compare each mutant line to the wild-type plants (Figure 3B-I). On average, a 2-fold increase in expression was measured for the genes *SND1*, *MYB46*, *VNI2*, *MYB83* and *MYB54* in the *swt16swt17* double mutant compared to the wild type (Figure 3B, C, D, F and G), while a similar tendency was observed for *MYB4*, *SND3* and *MYB103* expression (Figure 3E, H and I). Overall, these results

show that in the *swt16swt17* double mutant neither stem cell maintenance nor xylem identity genes are affected, whereas secondary cell wall biosynthesis genes are deregulated.

Next, we tested whether this transcriptional deregulation was accompanied by modifications in the cell wall composition. We used Fourier-transformed infrared spectroscopy (FTIR) on inflorescence stem cross-sections to analyze the xylem secondary cell wall composition as previously described in Le Hir et al. (2015) (Figure 4). The average spectra for all three mutants showed several differences compared to the wild-type spectra in fingerprint regions associated with cellulose, hemicelluloses and lignin (Figure 4A). The *t*-values, plotted against each wavenumber of the spectrum, showed that the mutant lines exhibited several significant negative and positive peaks (higher or lower absorbance than in the wild type) at wavenumbers associated with cellulosic and hemicellulosic polysaccharides (898 cm^{-1}, 995-1120 cm^{-1}, 1187 cm^{-1}, 1295 cm^{-1}, 1373 cm^{-1}, 1401 cm^{-1}, 1423 cm^{-1}, 1430 cm^{-1}, 1440 cm^{-1}, and 1485 cm^{-1}) (Åkerholm and Salmén, 2001; Kačuráková et al., 2002; Lahlali et al., 2015) (Figure 4A and B). More precisely, wavenumbers at 898 cm^{-1}, associated with the amorphous region of cellulose (Kačuráková et al., 2002), and at 1430 cm^{-1}, associated with crystalline cellulose (Åkerholm and Salmén, 2001), showed opposite and significant differences (Figure 4B). This suggests a potential defect in cellulose organization in the xylem secondary cell wall. Measurements of the cellulose C-O vibrations at a peak height at 1050 cm^{-1} (Lahlali et al., 2015) further indicate modifications of the cellulose composition in the cell wall of all the mutant lines (Figure 4C).

The *swt16* and *swt16swt17* mutant also displayed significant variations compared to the wild type at 1740 cm^{-1} (band specific for acetylated xylan; Gou et al. 2003) and 1369 cm^{-1} (deformation of C-H linkages in the methyl group *O*-acetyl moieties; Mohebby, 2008) suggesting modifications in xylan acetylation (Figure 4A and B). Furthermore, the hemicellulose peak height at 1740 cm^{-1} (C-O and C-C bond stretching) was significantly smaller in the *swt16* mutant suggesting less acetylated xylan (Figure 3D). Although the *swt17* single mutant was not distinguishable from the wild type, the *swt16swt17* double mutant had significantly fewer acetylated xylans than the wild type and the *swt16* single mutant (Figure 4D). The lignin-associated bands at 1510 cm^{-1} (Faix, 1991), 1520 cm^{-1} (Faix, 1991; Gou et al., 2008) and 1595 cm^{-1} also exhibited significant differences in the single and double mutants compared to the wild type plants (Figure 4B). Measurements of the lignin peak height ratio (1510/1595 cm^{-1}) showed that the secondary cell wall of the *swt16* single mutant contains

significantly more G-type lignin than that of the wild type, while only a tendency was measured in the cases of the *swt17* and the *swt16swt17* mutants (Figure 4E).

Overall, these results suggest that sugar export towards the cytosol mediated by SWEET16 and/or SWEET17 is required to provide the intermediates needed for the synthesis of cellulosic and hemicellulosic polysaccharides.

The hexose content is modified in the inflorescence stem of the *swt16swt17* double mutant

Assuming that SWEET16 and SWEET17 are sugar carriers, we wondered what would be the metabolic status of the inflorescence stem in the *swt16swt17* double mutant. We therefore used GC-MS to explore the global metabolomic profiles of the wild-type and the double *swt16swt17* mutant, identifying a total of 158 metabolites. In order to identify the subset of metabolites that best discriminate between the genotypes, we performed a sPLS-DA (Figure 5A). The resulting score plot clearly allows the two genotypes to be separated by the first dimension (Figure 5A). Among the metabolites selected by the sPLS-DA analysis, a subsequent *t*-test identified nine that were significantly different between wild type and the *swt16swt17* double mutant: allothreonine, benzoic acid, citraconic acid, cysteinylglycine, fructose, fumaric acid, glucose-6-phosphate, phytol and valine (Figure 5B and Supplemental Table 3). The relative quantities of benzoic acid, citraconic acid and fumaric acid (a component of the tricarboxylic cycle) were significantly reduced in the double mutant compared to the wild type (Supplemental Figure 3A, B and F). On the other hand, significant accumulation of cysteinylglycine (an intermediate in glutathione biosynthesis;(Hasanuzzaman et al., 2017), hexoses and hexose-phosphates (e.g. glucose-6-phosphate and fructose), amino acids (e.g. allothreonine and valine) and phytol (a chlorophyll component; (Gutbrod et al., 2019) was measured in the *swt16swt17* mutant compared to the wild-type stems (Supplemental Figure 3C, D, E, G, H and I). We further quantified the soluble sugars and starch content in both genotypes by enzymatic methods. Consistent with the metabolomics results, a significant accumulation of fructose in the double mutant was confirmed (Figure 5C). In addition, the glucose content was significantly increased in the stem of the double mutant (Figure 5C), while no variation in the sucrose and starch contents was observed (Figure 5C). Interestingly, the inflorescence stem of the *swt16swt17* double mutant accumulated mostly hexoses while no significant changes in glucose or sucrose were observed in the stem of the *swt16* and *swt17* single mutants (Supplemental Figure 4A). Although it was not significant, a tendency to accumulate glucose was observed in the single mutants (Supplemental Figure 4B). A significant increase in fructose

content was measured only in the *swt17* mutant compared to the wild type (Supplemental Figure 4C).

SWEET16 and SWEET17 proteins interact physically and are expressed in the xylem during its early development

To localize SWEET16 and SWEET17 in the inflorescence stem, we generated translational fusions between GFP and the N-terminus of *SWEET16* or *SWEET17* coding sequences under the control of their native promoters. The translational fusions were transferred into the respective knockout mutants in order to check their functionalities. We then looked at the radial growth of the inflorescence stem in the transgenic plants. *pSWT17:GFP-SWT17* successfully complemented the phenotype of the *swt17* mutant (Supplemental Figure 5), while *pSWT16:GFP-SWT16* only partially complemented the stem phenotype of the *swt16* mutant (Supplementary Figure 5). However, full complementation of the double mutant *swt16swt17* was achieved when both translational GFP fusions were expressed (Supplemental Figure 5). Unfortunately, despite the phenotype complementation, we could not detect any GFP signal in these lines. Previously, using lines expressing *pSWT:GUS* translational fusions, we showed that SWEET16 and SWEET17 were expressed in the xylem tissue of petioles and inflorescence stems (Chardon et al., 2013; Klemens et al., 2013). Here we completed this analysis by studying the expression patterns of SWEET16 and SWEET17 in cross sections from three different zones of the stem: (1) a stem region where the growth was rapid, (2) a stem region where elongation growth had finished but where further thickening of the secondary cell wall was still ongoing and (3) the base of the stem, which corresponds to a mature zone (Hall and Ellis, 2013) (Figure 6). Interestingly, the expression pattern of *SWEET16* and *SWEET17* varied depending on the developmental stages. The *SWEET16* expression pattern fluctuated more depending on the stage of inflorescence stem development (Figure 6A-C). In the region where the stem was growing rapidly (Figure 6A and inset) and in the region where secondary cell wall thickening was still ongoing (Figure 6B and inset), expression of *SWEET16* was observed in the interfascicular fibers, across the procambium-xylem boundary and in the young xylem vessels (Figure 6A-B and insets). Faint GUS staining was also observed in the phloem cells at these stages (Figure 6A-B). In the mature stem, *SWEET16* expression was restricted to the xylary parenchyma cells (Figure 6C). In contrast, *SWEET17* expression was restricted mostly to the xylem parenchyma cells present in the distal part of the vascular bundle (Figure 6D-F). Expression of *SWEET17* was also observed in the young xylem cells before extensive cell wall

lignification had occurred, as shown by the weaker phloroglucinol cell wall staining (Figure 6E, 6F and inset). Here, it is worth noting that we use the general term "young xylem cells" because it is not possible to know whether the GUS signal is present in developing xylary fibers and/or in developing xylem vessels. In conclusion, *SWEET16* and *SWEET17* expression patterns overlap in the young xylem cells as well as in the xylary parenchyma cells.

It has been established that plant sugar SWEET transporters require homo or hetero-oligomerization to gain functionality (Xuan et al., 2013). Because *SWEET16* and *SWEET17* expression patterns overlap in young xylem cells and xylary parenchyma cells, we investigated whether these proteins could interact. Xuan et al. (2013) previously showed that SWEET16 and SWEET17 can form homodimers as well as heterodimers in a split ubiquitin yeast two-hybrid assay. We confirmed that SWEET16 and SWEET17 can form a heterodimer at the vacuolar membrane in a bimolecular fluorescence complementation assay in Arabidopsis mesophyll protoplasts (Figure 6G-I).

DISCUSSION

To efficiently control carbon homeostasis within a cell and to fuel the different metabolic and signaling pathways, dynamic sugar storage in the plant vacuole is critical. Over the past years, several vacuolar transporters have been identified at the molecular level (for review see Hedrich et al., 2015). Among them, SWEET16 and SWEET17 have been characterized as bidirectional tonoplastic sugar facilitators and shown to be involved in seed germination, root growth and stress tolerance (Chardon et al., 2013; Klemens et al., 2013; Guo et al., 2014). In addition, the expression of both genes has been shown in the inflorescence stem's vascular parenchyma cells, but this had not previously been explored further. In this work, we ask whether facilitated sugar transport (*via* SWEET16 and SWEET17) across the vacuolar membrane limits vascular tissue development in the inflorescence stem of Arabidopsis.

First, our data highlight modifications of hexose homeostasis in the inflorescence stem of the different mutant lines. Although a tendency to accumulate glucose was observed in the *swt16* mutant, a significant increase in fructose was measured in the *swt17* mutant stem. Furthermore, mutations in both *SWEET16* and *SWEET17* induced somewhat specific accumulation of glucose, glucose-6-phosphate and fructose in the inflorescence stem. It has been previously shown that defects in the expression of vacuolar sugar transporters alter carbon partitioning and allocation in different organs, which is in line with our findings for the

inflorescence stem (Wingenter et al., 2010; Yamada et al., 2010; Poschet et al., 2011; Chardon et al., 2013; Klemens et al., 2013; Guo et al., 2014; Klemens et al., 2014). Knowing that SWEET proteins are sugar facilitators working along the concentration gradient (Chen et al., 2010) and that at least half of the hexoses are present in the plant vacuole (Heineke et al., 1994; Weiszmann et al., 2018), we can reasonably propose that some of the hexoses are trapped inside the vacuole in the single *swt16* and *swt17* mutants and the *swt16swt17* double mutant. As a consequence, modifications in the distribution of hexose concentrations between the vacuole and the cytosol, which would impact the availability of hexoses for subsequent metabolic and signaling purposes, could be expected. Hexoses are known to favor cell division and expansion, while sucrose favors differentiation and maturation (Koch, 2004). In addition, after metabolization, hexoses and hexoses-phosphates constitute the building blocks for the synthesis of cell wall polysaccharides (Verbančič et al., 2018). Since *SWEET16* and/or *SWEET17* are expressed in the xylem initials, in young xylem cells and in xylem parenchyma cells, we propose that enhanced storage of vacuolar hexoses in these cells will affect different stages of xylem development.

(Pro)cambium and xylem tissues can be regarded as sinks because they rely mostly on the supply of carbohydrates from the surrounding cells to sustain their development (Sibout et al., 2008; Spicer, 2014). In aspen stem, a gradual increase in sucrose and reducing sugars, together with a rise in the activities of sugar metabolism enzymes, are observed across the cambium-xylem tissues (Roach et al., 2017). In addition, in tomato, modification of fructose phosphorylation by the fructokinase SlFRK2 leads to a defect in cambium activity (Damari-Weissler et al., 2009). Taken together, these results support the need for maintenance of sugar homeostasis in the (pro)cambium to respond to the high metabolic activity required during cell division. Our work identified SWEET16 as a player in the dividing xylem cells, acting to balance the tradeoffs between the need for sugars in the cytosol and their storage in the vacuole (Figure 7). This conclusion is supported by the fact that *SWEET16* is expressed across the procambium-xylem boundary and that a mutation in *SWEET16* leads to defects in the number of xylem cells and in radial growth of the inflorescence stem. Furthermore, the expression of the gene coding for the WUSCHEL RELATED HOMEOBOX 4 (WOX4) transcription factor (Etchells et al., 2013), which is involved in cellular proliferation, was unchanged in both *swt16* and *sw16swt17* mutants. This suggest that the defects in xylem cell division result mostly from reduced availability of energy and matter resources due to a reduction in sugar transport, rather than from the signaling role of sugars. Finally, the partial complementation of the *swt16* mutant

could also suggest that other vacuolar sugar transporters, yet to be identified, might be at play in this process.

The reduced number of xylem vessels in the *swt16swt17* double mutant's vascular bundle could be explained by the upregulation of *VND-INTERACTING 2* (*VNI2*), which is a repressor of the activity of the master regulator of xylem vessel differentiation VND7 (Zhong et al., 2008; Yamaguchi et al., 2010). On the other hand, the overexpression in the double mutant *swt16swt17* of SECONDARY WALL-ASSOCIATED NAC DOMAIN 1 (SND1), the master switch for fiber differentiation, would be expected to result in a shift towards increased differentiation of xylary fibers (Zhong et al., 2006), which is not consistent with the fewer fibers observed in the double mutant. Based on these results, we can assume that the increase in storage of vacuolar hexoses in the double mutant also affects xylem cell differentiation. Against this hypothesis, our results show that both xylary fibers and xylem vessels number decreased proportionately, since no change in the xylem vessels/xylary fibers ratio was measured. Consistent with this observation, the expression of the gene coding for the PHLOEM INTERCALATED WITH XYLEM (PXY) receptor, which is involved in xylem cell differentiation (Etchells et al., 2016), was not modified. Despite the upregulation of *VNI2* and *SND1* expression, which could be due to a feedback mechanism yet to be identified, these results therefore tend to suggest that no disequilibrium is occurring in xylem cell differentiation in the *swt16swt17* mutant stem. The enhanced storage of hexoses in the vacuole of the double mutant is therefore affecting the overall pattern of xylem cell division rather than xylem cell differentiation.

After cell division and differentiation, xylem cells undergo a developmental program that includes secondary cell wall formation, lignification and programmed cell death, to produce functional xylem fibers and vessels (Schuetz et al., 2012) (Figure 7). Along with the overexpression of *SDN1*, the overexpression of genes encoding its downstream targets, namely MYB DOMAIN PROTEIN 46 and 83 (MYB46 and MYB83), was observed in the *swt16swt17* double mutant. Furthermore, the targets of the MYB46/MYB83 node, which positively regulates SND3 (SECONDARY WALL-ASSOCIATED NAC DOMAIN PROTEIN 3), KNAT7 (KNOTTED-LIKE HOMEOBOX OF ARABIDOPSIS THALIANA 7), MYB43 and MYB54 or/and negatively regulates MYB103, KNAT7 and MYB4, all of which are involved in the formation of the xylem secondary cell wall, are also upregulated (Hussey et al., 2013). KNAT7 directly or indirectly represses cellulose, hemicellulose and lignin biosynthetic genes (Li et al., 2012), while MYB54 is related to cellulose synthesis (Zheng et al., 2019). In

Arabidopsis, MYB43 along with other MYB transcription factors regulates lignin biosynthesis (Geng et al., 2020), while its ortholog in rice is involved in the regulation of cellulose deposition (Ambavaram et al., 2011). Finally, upregulation of MYB4 in Arabidopsis results in downregulation of the lignin pathway (Jin et al., 2000), while a role for MYB103 in lignin biosynthesis has been shown in Arabidopsis stem (Öhman et al., 2013). In the *swt16wt17* double mutant, these transcriptional changes were accompanied by modifications of the secondary cell wall in terms of cellulose and hemicellulose composition. However, a single mutation in *SWEET16* or *SWEET17* was sufficient to modify the composition of the xylem cell wall without any alteration in the expression of genes involved in secondary cell wall synthesis. Our data further show that the *SWEET16* and *SWEET17* expression patterns overlap in xylem cells that are building a secondary cell wall and that they form a heterodimer in Arabidopsis mesophyll protoplasts. We therefore postulate that the intermediate sugars required for the synthesis of cell wall polysaccharides come in part from the vacuole unloading mediated by SWEET16 and SWEET17 homo- and heterodimers (Figure 7). Previously, it has been shown that genes encoding vacuolar sugar facilitators are up-regulated during secondary cell wall formation in xylem vessels, while sugar facilitators expressed at the plasma membrane are down-regulated (Supplementary Figure 2) (Li et al., 2016), supporting the idea that secondary cell wall formation relies on sugar export from the vacuole. In the current model of cell wall synthesis, the cytosolic catabolism of sucrose is thought to be the main source of nucleotide sugars (e.g. UDP-glucose, UDP-galactose, GDP-mannose) that act as precursors for cellulose and hemicellulose synthesis (Verbančič et al., 2018). Our data support the existence of a more complex system in which the export of vacuolar hexoses also represents a source for the synthesis of nucleotide sugars and subsequent cell wall formation (Figure 7).

Because *SWEET16* and *SWEET17* are also expressed in the xylary parenchyma cells, we postulate that the maintenance of sugar homeostasis within this cell type, is important and could contribute to the provision of carbon skeletons for secondary cell wall synthesis after the disappearance of the vacuole from the maturing xylem cells (Figure 7). Within this scheme, the export of sugars in the apoplastic space between parenchyma cells and developing conducting cells could be carried out by the plasmalemmal SWEET11 and SWEET12 transporters which also expressed in the xylary parenchyma cells (Figure 7 and (Le Hir et al., 2015). Such cooperation between parenchyma cells and developing conducting cells was previously described as the “good neighbor” hypothesis in the context of H_2O_2 and monolignol transport (Barcelo, 2005; Smith et al., 2013; Smith et al., 2017). To further explore the importance of

443 sugar transport between xylary parenchyma cells and developing xylem cells, more
444 experiments, such as cell-specific complementation of the *sweet* mutant lines, will be needed
445 in order to better comprehend the role of xylary parenchyma cells in xylem development.

446 In conclusion, our work shows that exchange of intracellular hexoses, mediated by
447 SWEET16 and/or SWEET17 at the tonoplast, contributes to xylem development by regulating
448 the amounts of sugars that will be made available to the different cellular processes. However,
449 how the cell is prioritizing the distribution of sugars among the different processes remains an
450 open question. Although these technologies are challenging, the use of non-aqueous
451 fractionation and metabolomics approaches (Fürtauer et al., 2019) could help in resolving
452 subcellular sugar metabolism in a cell-specific context in mutant lines affected in sugar
453 metabolism, transport and signaling.

454

455

456

MATERIALS AND METHODS

Plant material and growth conditions

Seeds of T-DNA insertion lines homozygous for *SWEET17* (*sweet17-1*) and *SWEET16* (*sweet16-3* and *sweet16-4*) were gifts from Dr. F. Chardon and Pr. E. Neuhaus respectively. The *sweet17-1* line was previously reported to be a knock-out by Chardon et al. (2013). The *sweet16-3* (SM_3_1827) and *sweet16-4* (SM_3_30075) lines were numbered following the *sweet16-1* and *sweet16-2* lines already published by Guo et al. (2014). To verify whether *sweet16-3* and *sweet16-4* were knock-out mutants we performed RT-PCR with specific primers to amplify the full-length *SWEET16* cDNA (Supplemental Figure 1 and Supplemental Table 4). Since only the *sweet16-4* mutant turned to be a knock-out (Supplemental Figure 1B), we crossed it with *swt17-1* to obtained the double mutant *sweet16-4sweet17-1* (hereafter referred as *swt16swt17*). Homozygous plants were genotyped using gene-specific primers in combination with a specific primer for the left border of the T-DNA insertion (Supplemental Table 4).

To synchronize germination, seeds were stratified at 4°C for 48 hours and sown in soil in a growth chamber in long day conditions (16 hours day/8 hours night and 150 µE m^{-2} s^{-1}) at 22/18°C (day/night temperature) with 35% relative humidity. Plants were watered with Plant-Prod nutrient solution twice a week (Fertil, https://www.fertil.fr/). For all experiments, the main inflorescence stems (after removal of lateral inflorescence stems, flowers and siliques) were harvested from seven-week old plants.

Inflorescence stem sample preparation

For each plant, the main inflorescence stem height was measured with a ruler before harvesting a 1 to 2 cm segment taken at the bottom part of the stem. The stem segments were embedded in 8% agarose solution and sectioned with a VT100 S vibratome (Leica, https://www.leica-microsystems.com/). Some of the cross-sections were used for FT-IR analysis and the others were stained with a FASGA staining solution prepared as described in Tolivia and Tolivia (1987) for morphometric analysis of the xylem.

Morphometric analysis of the xylem

Previously stained inflorescence stem cross-sections were imaged under an Axio Zoom V16 microscope equipped with a Plan-Neofluar Z 2.3/0.57 FWD 10.6 objective (Zeiss, https://www.zeiss.fr/microscopie/). For each section, the diameter of the inflorescence stem was measured using the Image J software package (https://imagej.nih.gov/ij/). For the same sections all the vascular bundles were photographed individually using a confocal laser scanning microscope and morphological analysis of the xylem were performed as described in Le Hir et al. (2015). For each vascular bundle, the morphological segmentation made it possible to find the number of xylem cells (xylary fibers and xylem vessels) as well as their cross-sectional areas. Cells with a cross-sectional area of between 5 to 150 µm² were considered to be xylary fibers and cells with a cross-sectional area greater than 150 µm² were considered to be xylem vessels. The sum of all xylem cell cross-sectional areas was then calculated to give the total xylem cross-sectional area. The average xylary fiber and xylem vessel area was calculated by dividing the total xylem cross-sectional area by the number of each cell type.

FT-IR analysis of the xylem secondary cell wall

The composition of the secondary cell wall of the xylem tissue was determined by Fourier Transformed Infra-red spectroscopy using an FT-IR Nicolet^{TM} iN^{TM} (Thermo Fisher Scientific, https://www.thermofisher.com). Spectral acquisitions were done in transmission mode on a 30 µm by 30 µm acquisition area targeting the xylem tissue (xylem vessels and xylary fibers) as described in Le Hir et al. (2015). Between 10 to 15 acquisition points sweeping the xylem tissue homogeneously were performed on each vascular bundle within a stem section. Three individual inflorescence stems were analyzed for each genotype. After sorting the spectra and correcting the baseline, the spectra were area-normalized and the different genotypes were compared as described in Le Hir et al. (2015). The absorbance values (maximum height) of the major cellulose, lignin and hemicellulose bands in the fingerprint region (1800–800 cm^{-1}) were collected using TQ Analyst EZ edition (Thermo Fisher Scientific, https://www.thermofisher.com).

Metabolomic analysis

The inflorescence stems of the wild-type and the *swt16swt17* double mutant were harvested in the middle of the day (8 hours after the beginning of the light period). Metabolites were extracted from 4.5 mg of lyophilized stem powder from eight individual plants and analyzed by GC-MS as described in Cañas et al. (2020). Relative concentrations of metabolites were determined relative to the internal standard ribitol, which was added after grinding the lyophilized material. Differential accumulation of metabolites was determined by one-way analysis of variance (ANOVA) and *post hoc* Tukey tests ($P<0.05$).

Quantification of soluble sugars and starch

The main inflorescence stems of the wild type, and the *swt16*, *swt17* and *swt16swt17* mutants, were harvested in the middle of the day (8 hours after the beginning of the light period), frozen in liquid nitrogen and ground with a mortar and a pestle. Soluble sugars and starch were extracted from 50 mg of powder from an individual stem as described in Sellami et al. (2019). Depending on the experiment, 4 to 9 biological replicates were analyzed.

RNA isolation and cDNA synthesis

RNAs were prepared from the main inflorescence stem from four 7-week-old individual plants grown as described above. Samples were frozen in liquid nitrogen before being ground with a mortar and a pestle. Powders were stored at -80°C until use. Total RNA was extracted from frozen tissue using TRIzol® reagent (Thermo Fisher Scientific, 15595-026, https://www.thermofisher.com) and treated with DNase I, RNase-free (Thermo Fisher Scientific, EN0521, https://www.thermofisher.com). cDNA was synthetized by reverse transcribing 1 µg of total RNA using RevertAid H minus reverse transcriptase (Thermo Fisher Scientific, EP0452, https://www.thermofisher.com) with 1 µl of oligo(dT)18 primer (100 pmoles) according to the manufacturer's instructions. The reaction was stopped by incubation at 70 °C for 10 min.

Quantitative qPCR experiment

Transcript levels were assessed for four independent biological replicates in assays with triplicate reaction mixtures by using specific primers either designed with the Primer3 software (http://bioinfo.ut.ee/primer3-0.4.0/primer3/) or taken from the literature (Supplemental Table

5). qPCR reactions were performed in a 96-well transparent plate on a Bio-Rad CFX96 Real-Time PCR machine (Bio-Rad) in 10 µl mixtures each containing 5 µl of Takyon™ ROX SYBR® MasterMix dTTP Blue (Eurogentec, UF-RSMT-B0710, https://www.eurogentec.com/), 0.3 µl forward and reverse primer (30 µM each), 2.2 µl sterile water and 2.5 µl of a 1/30 dilution of cDNA. The following qPCR program was applied: initial denaturation at 95°C for 5 min, followed by thirty-nine cycles of 95°C for 10 sec, 60°C for 20 sec, 72°C for 30 sec. Melting curves were derived after each amplification by increasing the temperature in 0.5°C increments from 65°C to 95°C. The Cq values for each sample were acquired using the Bio-Rad CFX Manager 3.0 software package. The specificity of amplification was assessed for each gene, using dissociation curve analysis, by the precision of a unique dissociation peak. If one of the Cq values differed from the other two replicates by > 0.5, it was removed from the analysis. The amplification efficiencies of each primer pair were calculated from a 10-fold serial dilution series of cDNA (Supplemental Table 5). Four genes were tested as potential reference genes: *APT1* (At1g27450), *TIP41* (At4g34270), *EF1α* (At5g60390) and *UBQ5* (At3g62250). The geNorm algorithm (Vandesompele et al., 2002) was used to determine the gene most stably expressed among the different genotypes analyzed, namely *UBQ5* in this study. The relative expression level for each genotype was calculated according to the ΔCt method using the following formula: average $E_t^{-Cq(\text{of target gene in A})}/E_r^{-Cq(\text{of reference gene in A})}$, where E_t is the amplification efficiency of the target gene primers, E_r is the reference gene primer efficiency, A represents one of the genotypes analyzed.

Tagged protein constructs

For complementation of the single *sweet16-4* and *sweet17-1* and the double *sweet16-4sweet17-1* mutants, N terminal fusions with GFP were constructed as follow. First, the coding sequence of eGFP was amplified from the pKGWFS7 plasmid (Karimi et al., 2002) without a stop codon and then introduced into a modified donor pENTR vector to produce pENT-GFP (w/o stop). To make the N terminal translational GFP fusions (pSWEET16:GFP-SWEET16 and pSWEET17:GFP-SWEET17), the promoters (1295 bp for *SWEET16* and 2004 bp for *SWEET17*) and genomic sequences (1863 bp for *SWEET16* and 2601 bp for *SWEET17*) were amplified separately and then cloned on each side of the GFP gene in the intermediary vector pENT-GFP (w/o stop) by taking advantage of the restriction sites generated by PCR. All the PCR reactions were performed using Phusion High-Fidelity DNA Polymerase (Thermo Fisher Scientific, F-530S, https://www.thermofisher.com) with the primers listed in Supplemental

582 Table 4. Donor vectors created in this way were analyzed by sequencing in order to check the
583 reading frame of the translational fusions and the integrity of the whole genomic sequences.
584 Destination binary vectors were then obtained by recombination, using Gateway® LR Clonase
585 II Enzyme Mix (Thermo Fisher Scientific, 11791-100, https://www.thermofisher.com),
586 between pENTR donor vectors and pMDC123 for N terminal fusions (Curtis and Grossniklaus,
587 2003). All binary vectors were introduced into *Agrobacterium tumefaciens* C58pMP90 (Koncz
588 and Schell, 1986) by electroporation. Arabidopsis single mutants *swt16-4* and *swt17-1* as well
589 as the double mutant *sweet16-4sweet17-1* plants were transformed by the floral dip method
590 (Clough and Bent, 1998). Transformants were selected on hygromycin (15 mg/L) for pMDC99
591 constructs and/or Basta (7.5 mg/L) for pMDC123 constructs. For all constructs, three
592 independent transgenic lines were analyzed and one representative line was selected for
593 subsequent studies.

594 For the bimolecular fluorescence complementation (BiFC) assay, the full-length ORFs of
595 *SWEET16* and *SWEET17* were amplified from cDNA with the primers given in Supplemental
596 Table 4, either with or without their stop codons, depending on the final vector used. The ORFs
597 were further sub-cloned into pBlueScript II SK, blunt end cut with EcoRV. The resulting
598 vectors were checked for errors and orientation of the insert by sequencing with T3 and T7
599 primers. Subsequently, positive clones in the T7 orientation and the corresponding pSAT1
600 vectors (Lee et al., 2008) were cut with EcoRI and XhoI. *SWEET16* including the stop codon
601 was ligated into pSAT1-cCFP-C, and *SWEET17* without the stop codon into pSAT1-nCerulean-
602 N. Plasmid DNA of the final constructs was isolated with a PureLink™ HiPure Plasmid Filter
603 Midiprep Kit (Invitrogen™ /Thermo Fisher Scientific) according to the manufacturer's manual.
604 Isolation and transfection of Arabidopsis mesophyll protoplasts were performed as described
605 by Yoo et al. (2007). For imaging protoplasts, a Leica TCS SP5 II confocal laser scanning
606 microscope (http://www.leica-microsystems.com) was used. All pictures were taken using a
607 Leica HCX PL APO 63·/1.20 w motCORR CS objective with a VIS-Argon laser suitable for
608 constructs with CFP (Cerulean, 458 nm/480-520 nm) derivates.

609

610 ***Statistical analysis***

611 Differences between genotypes were assessed by a Student's *t*-test for comparison between
612 wild-type plants and mutant lines or by using one-way analysis of variance (ANOVA) with a
613 Tukey HSD post-hoc test. The sPLS-DA analysis was performed according to Jiang et al.

(2014) and Lê Cao et al. (2011). Irrelevant variables were removed using lasso (least absolute shrinkage and selection operator) penalizations and 20 variables were selected in each dimension. The 'mixOmics' package (Rohart et al., 2017) was used to perform sPLS-DA. All the statistical analysis and graph production were done in RStudio (version 1.1.456) (Rstudio Team, 2015), which incorporates the R software package (version 3.5.1) (R Core Team, 2017) using 'ggplot2' (Wickham, 2016), 'ggthemes' (Arnold, 2019), 'cowplot' (Wilke, 2019), 'hyperSpec' (Beleites and Sergo, 2020) and 'multcompView'(Graves et al., 2015).

AUTHOR CONTRIBUTIONS

Methodology, E.A., F.V. and F.Gi.; Resources, P.A.W. K., H.E.N, B.G. and F.Gu.; Investigation, E.A., B.H., F.V., P.A.W, F.G. and R.L.H.; Writing-Review & Editing, E.A., S.D., C.B. and R.L.H.; Conceptualization, R.L.H.; Supervision, R.L.H.; Funding acquisition, R.L.H.

ACKNOWLEDGMENTS

The authors would like to thank Dr. Fabien Chardon and Dr. Anne Krapp (IJPB, INRAE Versailles, France) for providing seeds of the *sweet17-1* mutant. The authors also thank Dr. Grégory Mouille (IJPB, INRAE Versailles, France) for advice on FTIR dataset analysis. This work has benefited from the support of IJPB's Plant Observatory technological platforms and from a French State grant (Saclay Plant Sciences, reference ANR-17-EUR-0007, EUR SPS-GSR) managed by the French National Research Agency under an Investments for the Future program (reference ANR-11-IDEX-0003-02) through PhD funding to E.A.

639 **REFERENCES**

640 **Åkerholm, M., and Salmén, L.** (2001). Interactions between wood polymers studied by
641 dynamic FT-IR spectroscopy. *Polymer (Guildf).* **42**:963–969.

642 **Ambavaram, M. M. R., Krishnan, A., Trijatmiko, K. R., and Pereira, A.** (2011).
643 Coordinated activation of cellulose and repression of lignin biosynthesis pathways in rice.
644 *Plant Physiol.* **155**:916–931.

645 **Arnold, J. B.** (2019). Ggthemes: extra themes, scales and geoms for "ggplot2" Advance Access
646 published 2019.

647 **Barcelo, R. A.** (2005). Xylem parenchyma cells deliver the H2O2 necessary for lignification
648 in differentiating xylem vessels. *Planta* **220**:747–756.

649 **Beleites, C., and Sergo, V.** (2020). hyperSpec: a package to handle hyperspectral data sets in
650 R. *CRAN Packag.* Advance Access published 2020.

651 **Cañas, R. A., Yesbergenova-Cuny, Z., Belanger, L., Rouster, J., Brulé, L., Gilard, F.,**
652 **Quilleré, I., Sallaud, C., and Hirel, B.** (2020). NADH-GOGAT overexpression does not
653 improve maize (Zea mays L.) performance even when pyramiding with NAD-IDH, GDH
654 and GS. *Plants* **9**.

655 **Chardon, F., Bedu, M., Calenge, F., Klemens, P. A. W., Spinner, L., Clement, G., Chietera,**
656 **G., Léran, S., Ferrand, M., Lacombe, B., et al.** (2013). Leaf fructose content is
657 controlled by the vacuolar transporter SWEET17 in *Arabidopsis*. *Curr. Biol.* **23**:697–702.

658 **Chen, L.-Q., Hou, B.-H., Lalonde, S., Takanaga, H., Hartung, M. L., Qu, X.-Q., Guo, W.-**
659 **J., Kim, J.-G., Underwood, W., Chaudhuri, B., et al.** (2010). Sugar transporters for
660 intercellular exchange and nutrition of pathogens. *Nature* **468**:527–532.

661 **Chen, L.-Q., Qu, X.-Q., Hou, B.-H., Sosso, D., Osorio, S., Fernie, A. R., and Frommer, W.**
662 **B.** (2012). Sucrose efflux mediated by SWEET proteins as a key step for phloem transport.
663 *Science (80-.).* **335**:207–211.

664 **Clough, S. J., and Bent, A. F.** (1998). Floral dip: A simplified method for Agrobacterium-
665 mediated transformation of *Arabidopsis thaliana*. *Plant J.* **16**:735–743.

666 **Curtis, M. D., and Grossniklaus, U.** (2003). A gateway cloning vectors set for high-
667 throughput functional analysis of genes in planta. *Plant Physiol.* **133**:462–469.

668 **Damari-Weissler, H., Rachamilevitch, S., Aloni, R., German, M. A., Cohen, S.,**
669 **Zwieniecki, M. A., Holbrook, N. M., and Granot, D.** (2009). LeFRK2 is required for
670 phloem and xylem differentiation and the transport of both sugar and water. *Planta*
671 **230**:795–805.

672 **Dinant, S., Wolff, N., De Marco, F., Vilaine, F., Gissot, L., Aubry, E., Sandt, C., Bellini,**
673 **C., and Le Hir, R.** (2019). Synchrotron FTIR and Raman spectroscopy provide unique
674 spectral fingerprints for *Arabidopsis* floral stem vascular tissues. *J. Exp. Bot.* **70**:871–884.

675 **Etchells, J. P., Provost, C. M., Mishr, L., and Turner, S. R.** (2013). WOX4 and WOX14 act
676 downstream of the PXY receptor kinase to regulate plant vascular proliferation
677 independently of any role in vascular organisation. *Dev.* **140**:2224–2234.

678 **Etchells, J. P., Smit, M. E., Gaudinier, A., Williams, C. J., and Brady, S. M.** (2016). A brief
679 history of the TDIF-PXY signalling module: Balancing meristem identity and
680 differentiation during vascular development. *New Phytol.* **209**:474–484.

681 **Eveland, A. L., and Jackson, D. P.** (2012). Sugars, signalling, and plant development. *J. Exp.*
682 *Bot.* **63**:3367–3377.

683 **Faix, O.** (1991). Classification of lignins from different botanical origins by FT-IR
684 spectroscopy. *Holzforschung-International J. Biol. Chem. Phys. Technol. Wood* **45**:21–27.

685 **Fukuda, H., and Ohashi-Ito, K.** (2019). *Vascular tissue development in plants*. 1st ed. Elsevier
686 Inc.

687 **Fürtauer, L., Küstner, L., Weckwerth, W., Heyer, A. G., and Nägele, T.** (2019). Resolving
688 subcellular plant metabolism. *Plant J.* Advance Access published 2019,
689 doi:10.1111/tpj.14472.

690 **Furze, M. E., Trumbore, S., and Hartmann, H.** (2018). Detours on the phloem sugar
691 highway: stem carbon storage and remobilization. *Curr. Opin. Plant Biol.* **43**:89–95.

692 **Geng, P., Zhang, S., Liu, J., Zhao, C., Wu, J., Cao, Y., Fu, C., Han, X., He, H., and Zhao,**
693 **Q.** (2020). MYB20, MYB42, MYB43, and MYB85 regulate phenylalanine and lignin
694 biosynthesis during secondary cell wall formation1[OPEN]. *Plant Physiol.* **182**:1272–
695 1283.

696 **Gou, J. Y., Park, S., Yu, X. H., Miller, L. M., and Liu, C. J.** (2008). Compositional
697 characterization and imaging of "wall-bound" acylesters of Populus trichocarpa reveal

698 differential accumulation of acyl molecules in normal and reactive woods. *Planta* **229**:15–
699 24.

700 **Gould, N., Thorpe, M. R., Pritchard, J., Christeller, J. T., Williams, L. E., Roeb, G.,**
701 **Schurr, U., and Minchin, P. E. H.** (2012). AtSUC2 has a role for sucrose retrieval along
702 the phloem pathway: Evidence from carbon-11 tracer studies. *Plant Sci.* **188**–**189**:97–101.

703 **Graves, S., Piepho, H.-P., Selzer, L., and Dorai-Raj, S.** (2015). multcompView:
704 Visualizations of paired comparisons Advance Access published 2015.

705 **Guo, W.-J., Nagy, R., Chen, H.-Y., Pfrunder, S., Yu, Y.-C., Santelia, D., Frommer, W. B.,**
706 **and Martinoia, E.** (2014). SWEET17, a facilitative transporter, mediates fructose
707 transport across the tonoplast of Arabidopsis roots and leaves. *Plant Physiol.* **164**:777–
708 789.

709 **Gutbrod, K., Romer, J., and Dörmann, P.** (2019). Phytol metabolism in plants. *Prog. Lipid*
710 *Res.* **74**:1–17.

711 **Hall, H., and Ellis, B.** (2013). Transcriptional programming during cell wall maturation in the
712 expanding Arabidopsis stem. *BMC Plant Biol.* **13**:14.

713 **Hasanuzzaman, M., Nahar, K., Anee, T. I., and Fujita, M.** (2017). Glutathione in plants:
714 biosynthesis and physiological role in environmental stress tolerance. *Physiol. Mol. Biol.*
715 *Plants* **23**:249–268.

716 **Hedrich, R., Sauer, N., and Neuhaus, H. E.** (2015). Sugar transport across the plant vacuolar
717 membrane: Nature and regulation of carrier proteins. *Curr. Opin. Plant Biol.* Advance
718 Access published 2015, doi:10.1016/j.pbi.2015.04.008.

719 **Heineke, D., Wildenberger, K., Sonnewald, U., Willmitzer, L., and Heldt, H. W.** (1994).
720 Accumulation of hexoses in leaf vacuoles: Studies with transgenic tobacco plants
721 expressing yeast-derived invertase in the cytosol, vacuole or apoplasm. *Planta* **194**:29–33.

722 **Hussey, S. G., Mizrachi, E., Creux, N. M., and Myburg, A. A.** (2013). Navigating the
723 transcriptional roadmap regulating plant secondary cell wall deposition. *Front. Plant Sci.*
724 **4**:1–21.

725 **Jiang, M., Wang, C., Zhang, Y., Feng, Y., Wang, Y., and Zhu, Y.** (2014). Sparse partial-
726 least-squares discriminant analysis for different geographical origins of salvia miltiorrhiza
727 by 1h-nmr-based metabolomics. *Phytochem. Anal.* **25**:50–58.

728 **Jin, H., Cominelli, E., Bailey, P., Parr, A., Mehrtens, F., Jones, J., Tonelli, C., Wiesshaar,**
729 **B., and Martin, C.** (2000). Transcriptional repression by AtMYB4 controls production of
730 UV-protecting sunscreens in Arabidopsis. *EMBO J.* **19**:6150–6161.

731 **Kačuráková, M., Smith, A. C., Gidley, M. J., and Wilson, R. H.** (2002). Molecular
732 interactions in bacterial cellulose composites studied by 1D FT-IR and dynamic 2D FT-
733 IR spectroscopy. *Carbohydr. Res.* **337**:1145–1153.

734 **Karimi, M., Inze, D., and Depicker, A.** (2002). GATEWAY((TM)) vectors for
735 Agrobacterium-mediated plant transformation. *Trends Plant Sci.* **7**:193–195.

736 **Klemens, P. A. W., Patzke, K., Deitmer, J., Spinner, L., Le Hir, R., Bellini, C., Bedu, M.,**
737 **Chardon, F., Krapp, A., and Neuhaus, H. E.** (2013). Overexpression of the vacuolar
738 sugar carrier *AtSWEET16* modifies germination, growth, and stress tolerance in
739 Arabidopsis. *Plant Physiol.* **163**:1338–1352.

740 **Klemens, P. A. W., Patzke, K., Trentmann, O., Poschet, G., Büttner, M., Schulz, A.,**
741 **Marten, I., Hedrich, R., and Neuhaus, H. E.** (2014). Overexpression of a proton-coupled
742 vacuolar glucose exporter impairs freezing tolerance and seed germination. *New Phytol.*
743 **202**:188–197.

744 **Koch, K. E.** (2004). Sucrose metabolism: regulatory mechanisms and pivotal roles in suger
745 sensing and plant development. *Curr. Opin. Plant Biol.* **7**:235–246.

746 **Koncz, C., and Schell, J.** (1986). The promoter of TL-DNA gene 5 controls the tissue-specific
747 expression of chimaeric genes carried by a novel type of Agrobacterium binary vector.
748 *Mol. Gen. Genet.* **204**:383–396.

749 **Lahlali, R., Karunakaran, C., Wang, L., Willick, I., Schmidt, M., Liu, X., Borondics, F.,**
750 **Forseille, L., Fobert, P. R., Tanino, K., et al.** (2015). Synchrotron based phase contrast
751 X-ray imaging combined with FTIR spectroscopy reveals structural and biomolecular
752 differences in spikelets play a significant role in resistance to Fusarium in wheat. *BMC*
753 *Plant Biol.* **15**.

754 **Lê Cao, K. A., Boitard, S., and Besse, P.** (2011). Sparse PLS discriminant analysis:
755 Biologically relevant feature selection and graphical displays for multiclass problems.
756 *BMC Bioinformatics* **12**.

757 **Le Hir, R., Spinner, L., Klemens, P. A. W., Chakraborti, D., De Marco, F., Vilaine, F.,**

Wolff, N., Lemoine, R., Porcheron, B., Géry, C., et al. (2015). Disruption of the Sugar Transporters AtSWEET11 and AtSWEET12 Affects Vascular Development and Freezing Tolerance in *Arabidopsis*. *Mol. Plant* **8**:1687–1690.

Lee, L. Y., Fang, M. J., Kuang, L. Y., and Gelvin, S. B. (2008). Vectors for multi-color bimolecular fluorescence complementation to investigate protein-protein interactions in living plant cells. *Plant Methods* **4**:1–11.

Li, E., Bhargava, A., Qiang, W., Friedmann, M. C., Forneris, N., Savidge, R. A., Johnson, L. A., Mansfield, S. D., Ellis, B. E., and Douglas, C. J. (2012). The Class II KNOX gene KNAT7 negatively regulates secondary wall formation in Arabidopsis and is functionally conserved in Populus. *New Phytol.* **194**:102–115.

Li, Z., Omranian, N., Neumetzler, L., wang, ting, Herter, T., Usadel, B., Demura, T., Giavalisco, P., Nikoloski, Z., and Persson, S. (2016). A Transcriptional and Metabolic Framework for Secondary Wall Formation in Arabidopsis. *Plant Physiol.* Advance Access published 2016, doi:10.1104/pp.16.01100.

Lucas, W. J., Groover, A., Lichtenberger, R., Furuta, K., Yadav, S. R., Helariutta, Y., He, X. Q., Fukuda, H., Kang, J., Brady, S. M., et al. (2013). The Plant Vascular System: Evolution, Development and Functions. *J. Integr. Plant Biol.* **55**:294–388.

Mahboubi, A., Ratke, C., Gorzsás, A., Kumar, M., Mellerowicz, E. J., and Niittylä, T. (2013). Aspen SUCROSE TRANSPORTER3 allocates carbon into wood fibers. *Plant Physiol.* **163**:1729–1740.

Marriott, P. E., Gómez, L. D., and Mcqueen-Mason, S. J. (2016). Unlocking the potential of lignocellulosic biomass through plant science. *New Phytol.* **209**:1366–1381.

Martinoia, E. (2018). Vacuolar transporters - Companions on a longtime journey. *Plant Physiol.* **176**:pp.01481.2017.

Minchin, P. E. H., and McNaughton, G. S. (1987). Xylem transport of recently fixed carbon within lupin. *Aust. J. Plant Physiol.* **14**.

Mohebby, B. (2008). Application of ATR infrared spectroscopy in wood acetylation. *J. Agric. Sci. Technol.* **10**:253–259.

Öhman, D., Demedts, B., Kumar, M., Gerber, L., Gorzsás, A., Goeminne, G., Hedenström, M., Ellis, B., Boerjan, W., and Sundberg, B. (2013). MYB103 is required for

788 FERULATE-5-HYDROXYLASE expression and syringyl lignin biosynthesis in
789 Arabidopsis stems. *Plant J.* **73**:63–76.

790 **Payyavula, R. S., Tay, K. H. C., Tsai, C.-J., and Harding, S. A.** (2011). The sucrose
791 transporter family in Populus: the importance of a tonoplast PtaSUT4 to biomass and
792 carbon partitioning. *Plant J.* **65**:757–770.

793 **Poschet, G., Hannich, B., Raab, S., Jungkunz, I., Klemens, P. A. W., Krueger, S., Wic, S.,**
794 **Neuhaus, H. E., and Buttner, M.** (2011). A Novel Arabidopsis Vacuolar Glucose
795 Exporter Is Involved in Cellular Sugar Homeostasis and Affects the Composition of Seed
796 Storage Compounds. *Plant Physiol.* **157**:1664–1676.

797 **R Core Team** (2017). R: a language and environment for statistical computing. Advance
798 Access published 2017.

799 **Roach, M., Arrivault, S., Mahboubi, A., Krohn, N., Sulpice, R., Stitt, M., and Niittylä, T.**
800 (2017). Spatially resolved metabolic analysis reveals a central role for transcriptional
801 control in carbon allocation to wood. *J. Exp. Bot.* **68**:3529–3539.

802 **Rohart, F., Gautier, B., Singh, A., and Lê Cao, K. A.** (2017). mixOmics: An R package for
803 'omics feature selection and multiple data integration. *PLoS Comput. Biol.* **13**:1–19.

804 **Rstudio Team** (2015). RStudio: Integrated Development for R. Advance Access published
805 2015.

806 **Sakr, S., Wang, M., Dédaldéchamp, F., Perez-Garcia, M.-D., Ogé, L., Hamama, L., and**
807 **Atanassova, R.** (2018). The Sugar-Signaling Hub: Overview of Regulators and
808 Interaction with the Hormonal and Metabolic Network. *Int. J. Mol. Sci.* **19**:2506.

809 **Schuetz, M., Smith, R., and Ellis, B.** (2012). Xylem tissue specification, patterning, and
810 differentiation mechanisms. *J. Exp. Bot.* **64**:11–31.

811 **Sellami, S., Le Hir, R., Thorpe, M. R., Vilaine, F., Wolff, N., Brini, F., and Dinant, S.**
812 (2019). Salinity effects on sugar homeostasis and vascular anatomy in the stem of the
813 *Arabidopsis thaliana* inflorescence. *Int. J. Mol. Sci.* **20**:3167.

814 **Sibout, R., Plantegenet, S., and Hardtke, C. S.** (2008). Flowering as a Condition for Xylem
815 Expansion in *Arabidopsis* Hypocotyl and Root. *Curr. Biol.* **18**:458–463.

816 **Smetana, O., Mäkilä, R., Lyu, M., Amiryousefi, A., Rodríguez, F. S., Wu, M., Solé-gil, A.,**

Gavarrón, M. L., Siligato, R., Miyashima, S., et al. (2019). High levels of auxin signalling define the stem-cell organizer of the vascular cambium. *Nature* **565**:485–491.

Smit, M., McGregor, S., Sun, H., Gough, C., Bågman, A.-M., Soyars, C. L., Kroon, J. T. M., Gaudinier, A., Williams, C. J., Yang, X., et al. (2019). A PXY-Mediated Transcriptional Network Integrates Signaling Mechanisms to Control Vascular Development in Arabidopsis. *Plant Cell* Advance Access published 2019, doi:10.1105/tpc.19.00562.

Smith, R. A., Schuetz, M., Roach, M., Mansfield, S. D., Ellis, B., and Samuels, L. (2013). Neighboring parenchyma cells contribute to *Arabidopsis* xylem lignification, while lignification of interfascicular fibers is cell autonomous. *Plant Cell* **25**:3988–3999.

Smith, R. A., Schuetz, M., Karlen, S. D., Bird, D., Tokunaga, N., Sato, Y., Mansfield, S. D., Ralph, J., and Samuels, A. L. (2017). Defining the diverse cell populations contributing to lignification in *Arabidopsis thaliana* stems. *Plant Physiol.* **174**:1028–1036.

Spicer, R. (2014). Symplasmic networks in secondary vascular tissues: Parenchyma distribution and activity supporting long-distance transport. *J. Exp. Bot.* **65**:1829–1848.

Tolivia, D., and Tolivia, J. (1987). Fasga: A new polychromatic method for simultaneous and differential staining of plant tissues. *J. Microsc.* **148**:113–117.

Truernit, E., and Sauer, N. (1995). The promoter of the Arabidopsis thaliana SUC2 sucrose-H+ symporter gene directs expression of B-glucuronidase to the phloem: evidence for phloem loading and unloading by SUC2. *Planta* **196**:564–570.

Vandesompele, J., De Preter, K., Pattyn, F., Poppe, B., Van Roy, N., De Paepe, A., and F., S. (2002). Accurate normalization of real-time quantitative RT-PCR data by geometric averaging of multiple internal control genes. *Genome Biol.* **3**:research0034.1-0034.11.

Verbančič, J., Lunn, J. E., Stitt, M., and Persson, S. (2018). Carbon supply and the regulation of cell wall synthesis. *Mol. Plant* **11**:75–94.

Weiszmann, J., Fürtauer, L., Weckwerth, W., and Nägele, T. (2018). Vacuolar sucrose cleavage prevents limitation of cytosolic carbohydrate metabolism and stabilizes photosynthesis under abiotic stress. *FEBS J.* Advance Access published 2018, doi:10.1111/febs.14656.

Wickham, H. (2016). *ggplot2: Elegant Graphics for Data Analysis*. New York: Springer-

847 Verlag.

848 **Wilke, C. O.** (2019). Cowplot: streamlined plot theme and plot annotation for "ggplot2"
849 Advance Access published 2019.

850 **Wingenter, K., Schulz, A., Wormit, A., Wic, S., Trentmann, O., Hoermiller, I. I., Heyer,**
851 **A. G., Marten, I., Hedrich, R., and Neuhaus, H. E.** (2010). Increased Activity of the
852 Vacuolar Monosaccharide Transporter TMT1 Alters Cellular Sugar Partitioning, Sugar
853 Signaling, and Seed Yield in Arabidopsis. *Plant Physiol.* **154**:665–677.

854 **Xuan, Y. H., Hu, Y. B., Chen, L.-Q., Sosso, D., Ducat, D. C., Hou, B.-H., and Frommer,**
855 **W. B.** (2013). Functional role of oligomerization for bacterial and plant SWEET sugar
856 transporter family. *Proc. Natl. Acad. Sci.* **110**:E3685–E3694.

857 **Yamada, K., Osakabe, Y., Mizoi, J., Nakashima, K., Fujita, Y., Shinozaki, K., and**
858 **Yamaguchi-Shinozaki, K.** (2010). Functional analysis of an Arabidopsis thaliana abiotic
859 stress-inducible facilitated diffusion transporter for monosaccharides. *J. Biol. Chem.*
860 **285**:1138–1146.

861 **Yamaguchi, M., Ohtani, M., Mitsuda, N., Kubo, M., Ohme-Takagi, M., Fukuda, H., and**
862 **Demura, T.** (2010). VND-INTERACTING2, a NAC Domain Transcription Factor,
863 Negatively Regulates Xylem Vessel Formation in Arabidopsis. *Plant Cell* **22**:1249–1263.

864 **Yoo, S. D., Cho, Y. H., and Sheen, J.** (2007). Arabidopsis mesophyll protoplasts: A versatile
865 cell system for transient gene expression analysis. *Nat. Protoc.* **2**:1565–1572.

866 **Zheng, M., Liu, X., Lin, J., Liu, X., Wang, Z., Xin, M., Yao, Y., Peng, H., Zhou, D. X., Ni,**
867 **Z., et al.** (2019). Histone acetyltransferase GCN5 contributes to cell wall integrity and salt
868 stress tolerance by altering the expression of cellulose synthesis genes. *Plant J.* **97**:587–
869 602.

870 **Zhong, R., Demura, T., and Ye, Z.-H.** (2006). SND1, a NAC Domain Transcription Factor,
871 Is a Key Regulator of Secondary Wall Synthesis in Fibers of Arabidopsis. *Plant Cell*
872 *Online* **18**:3158–3170.

873 **Zhong, R., Lee, C., Zhou, J., McCarthy, R. L., and Ye, Z.-H.** (2008). A Battery of
874 Transcription Factors Involved in the Regulation of Secondary Cell Wall Biosynthesis in
875 Arabidopsis. *Plant Cell* **20**:2763–2782.

876

877 **FIGURE LEGENDS**

878 **Figure 1. Altered development of the inflorescence stem in the *swt16swt17* double mutant.**

879 (A) Transverse sections of the basal part of the inflorescence stem of 7-week-old plants stained
880 with FASGA solution. Bars = 200 µm.
881 (B-F) Boxplots showing the inflorescence stem cross-sectional area (B), the area occupied by
882 xylem tissue (C) or phloem tissue (D) within a stem section, the ratio of xylem area to stem area
883 (E) and the ratio of phloem area to stem area (F).
884 The box and whisker plots represent values from 7 to 8 independent plants. The lines represent
885 median values, the tops and bottoms of the boxes represent the first and third quartiles
886 respectively, and whisker extremities represent maximum and minimum data points. A one-
887 way analysis of variance combined with the Tukey's comparison post-hoc test were performed.
888 Values marked with the same letter were not significantly different from each other, whereas
889 different letters indicate significant differences ($P < 0.05$).

890

891 **Figure 2. Knockout of *SWEET16* gene expression impacts the proliferation of xylem cells.**

892 (A to I) Boxplots showing the inflorescence stem height (A) and diameter (B), the ratio of vessel
893 number to fiber number (C), the cross-sectional area occupied by xylem tissue per vascular
894 bundle (D), the average cross-sectional area of a xylary fiber (E) or of a xylem vessel (F), and
895 the average number of xylem cells (G), of xylary fiber vessels (H) and of xylem vessels (I) per
896 vascular bundle.
897 The box and whisker plots represent values from 5 to 7 independent plants (A and B) or from
898 71, 53, 41 and 50 individual vascular bundles from wild type, *swt16*, *swt17* and *swt16swt17*
899 respectively taken from 5-7 independent plants for each genotype (C-I). The lines represent
900 median values, the tops and bottoms of the boxes represent the first and third quartiles
901 respectively, and whisker extremities represent maximum and minimum data points. Stars
902 denote significant differences between the mutant lines compared to the wild type according to
903 a Student's *t*-test (* $P<0.05$).

904

905 **Figure 3. Genes involved in the development of xylem secondary cell wall are deregulated**
906 **in the *swt16swt17* double mutant.**

907 (A to I) The mRNAs were extracted from total inflorescence stems collected from 7-week-old
908 wild-type, *swt16*, *swt17* and *swt16swt17* plants. The mRNA contents are expressed relative to
909 those of the reference gene *UBQ5*.

910 (A) Heatmap of expression of candidate genes involved in xylem development and secondary
911 cell wall biosynthesis in the inflorescence stem of the wild type, *swt16*, *swt17* and *swt16swt17*
912 mutants. The values used to build the heatmap are the mean accumulation of transcripts (n=4)
913 normalized by the median value of each gene and expressed as $\log_2$ values. For each gene, the
914 result of one-way ANOVA is displayed beside the heatmap. Those p-values below the
915 significance threshold (P<0.05) are in red.

916 (B to I) Boxplots showing the relative expression of *SND1* (B), *MYB46* (C), *VNI2* (D), *MYB4*
917 (E), *MYB83* (F), *MYB54* (G), *SND3* (H) and *MYB103* (I). The box-and-whisker plots represent
918 values from 4 biological replicates. The lines represent median values, the tops and bottoms of
919 the boxes represent the first and third quartiles respectively, and the ends of the whiskers
920 represent maximum and minimum data points. Black dots are outliers. Stars denote significant
921 differences between the mutant line compared to the wild type according to a Student's t-test (*
922 P<0.05; ** P<0.01; *** P<0.001). The experiment was repeated twice and gave similar results.

923

924 **Figure 4. The composition of the xylem secondary cell wall is altered in the *swt16swt17***
925 **double mutant.**
926 FTIR spectra were acquired on xylem tissue from sections of the basal part of the inflorescence
927 stem. All spectra were baseline-corrected and area-normalized in the range 1800-800 cm^{-1}.
928 (A) Average FTIR spectra were generated from 266, 170, 123 and 170 spectra for the wild type,
929 *swt16*, *swt17* and *swt16swt17* respectively, obtained using three independent plants for each
930 genotype.
931 (B) Comparison of FTIR spectra obtained from xylem cells of the *swt16*, *swt17*, and *swt16swt17*
932 mutants. A Student's t-test was performed to compare the absorbances for the wild type, single
933 and double mutants. The results were plotted against the corresponding wavenumbers. T-values
934 (vertical axis) between -2 and +2 correspond to non-significant differences (p-value < 0.05)
935 between the genotypes tested (n=3). T-values above +2 or below -2 correspond to, respectively,
936 significantly weaker or stronger absorbances in the mutant spectra relative to the wild type.
937 (C to E) Boxplots of the cellulose (C-O vibration band at 1050 cm^{-1}) (C), hemicellulose (C-O
938 and C-C bond stretching at 1740 cm^{-1}) (D) peak height and lignin peak height ratio (1510/1595

939 cm^{-1}) (E). The lines represent median values, the tops and bottoms of the boxes represent the
940 first and third quartiles respectively, and the ends of the whiskers represent maximum and
941 minimum data points. The boxplots represent values (shown as colored dots) from 266, 170,
942 123 and 170 spectra from the wild type, *swt16*, *swt17* and *swt16swt17* respectively, obtained
943 from three independent plants for each genotype. A one-way analysis of variance combined
944 with the Tukey's comparison post-hoc test were performed. Values marked with the same letter
945 were not significantly different from each other, whereas different letters indicate significant
946 differences ($P < 0.05$).
947

948 **Figure 5. Hexoses accumulate in the inflorescence stem of the *swt16swt17* double mutant.**

949 (A and B) Multivariate analysis of the metabolomic datasets obtained from wild-type and
950 *swt16swt17* inflorescence stems. Metabolites were extracted from eight individual plants for
951 each genotype and analyzed by GC-MS. Plants were grown under long-day conditions for seven
952 weeks. (A) sPLS-DA score plot for wild-type (purple) and *swt16swt17* (green) samples. The
953 variable plot of the sPLS-DA is presented in (B) and metabolites in red are significantly
954 different between the wild type and the *swt16swt17* mutant according to Student's *t*-test
955 ($P<0.05$) (Supplemental Table 3). ADP: adenosine-5-diphosphate; G-6-P: glucose-6-
956 phosphate.

957 (C) Boxplots showing the sucrose, glucose, fructose and starch contents in the inflorescence
958 stems of the wild type (in purple) and the *swt16swt17* (in green) mutant grown under long-day
959 conditions for seven weeks. The box-and-whisker plots represent values from 9 biological
960 replicates coming from plants grown at two separated times. The lines represent median values,
961 the tops and bottoms of the boxes represent the first and third quartiles respectively, and the
962 ends of the whiskers represent maximum and minimum data points. Black dots are outliers.
963 Asterisks above the boxes indicate statistical differences between genotypes according to
964 Student's *t*-test ($P<0.05$).

965

966 **Figure 6. *SWEET16* and *SWEET17* expression patterns vary during inflorescence stem**
967 **development and the two proteins interact physically.**

968 (A to C) *pSWEET16:GUS* expression pattern in sections taken at different positions in the
969 inflorescence stem of 8-week-old plants. (D to F) *pSWEET17:GUS* expression pattern in

970 sections taken at different positions in the inflorescence stem section of 8-week-old plants.
971 Sections were taken in a stem region where the growth was still rapid (A, D and inset), in a
972 stem region where elongation growth had finished but where thickening of the secondary cell
973 wall was still ongoing (B, E and inset), and at the bottom of the stem, a region that corresponds
974 to a mature stem (C, F and inset). Arrows point to cells showing blue GUS staining and asterisks
975 indicate xylary parenchyma cells. Lignin is colored pink after phloroglucinol staining. The
976 intensity of the pink color is correlated with the stage of lignification of the xylary vessels. ep:
977 epidermis; co: cortex; iff: interfascicular fibers; ph: phloem; xy: xylem.

978 (G to I) Fluorescence in an Arabidopsis mesophyll protoplast expressing *SWEET16:cCFP-C*
979 and *SWEET17:nCerulean-C* revealed by false color cyan (G). Chloroplast auto-fluorescence is
980 in false color red (H). Merge of (G) and (H) and bright field image (I). Invaginations around
981 the chloroplasts in (G) and (I) indicate that SWEET16 and SWEET17 interact at the vacuolar
982 membrane. Scale bar = 17 µm.

983

984 **Figure 7. Model for the role of SWEET transporters during xylem development in**
985 **Arabidopsis inflorescence stems.**
986 This model is based on the results presented in this work on SWEET16 and SWEET17 and
987 those previously published on SWEET11, SWEET12 and SUC2 transporters (Truernit and
988 Sauer, 1995; Chen et al., 2012; Gould et al., 2012; Le Hir et al., 2015). In the phloem tissue,
989 sucrose and hexoses present in the phloem parenchyma cells (PPC) are exported into the
990 apoplastic space between PPC and companion cells (CC) by the sugar transporters SWEET11
991 and SWEET12 (fuchsia circles). Apoplastic sucrose is then imported into the CC cytosol *via*
992 the SUC2 transporter (yellow circles) before entering the phloem sieve tubes (SE) and being
993 transported over long distances (light green arrows). A part of these sugars leaks from the SE,
994 most probably through plasmodesmata (orange arrow), and reaches axial sinks (e.g.
995 procambium and xylem) while another part of the sugars is reimported inside the SE, mostly
996 through the action of SUC2 (1). In the cells at the cambium-xylem boundary, soluble sugars are
997 probably exported by SWEET16 (light blue circles) into the cytosol in order to sustain the
998 division of xylem cells (2). Given the high cytosolic sugar demand required to sustain the
999 secondary cell wall (SCW) deposition process (3), sugars stored in the vacuole are likely
1000 exported into the cytosol through the action of SWEET16 (purple circles) and/or SWEET17
1001 (green circles). Interaction between SWEET16 and SWEET17 is shown as bicolor circles. After
1002 the completion of programmed cell death (PCD) and the disintegration of the vacuole (4), the

SCW is still being reinforced (5) and we can assume that the sugar demand is still high. At this stage, the sugars stored in the vacuole of the xylary parenchyma cells (XPC) are likely released by SWEET16 and/or SWEET17 and then exported into the apoplastic space by SWEET11 and SWEET12. Whether it is the sugars themselves or more complex cell wall sugar-derived molecules that reach the dead xylem cells remains an open question.

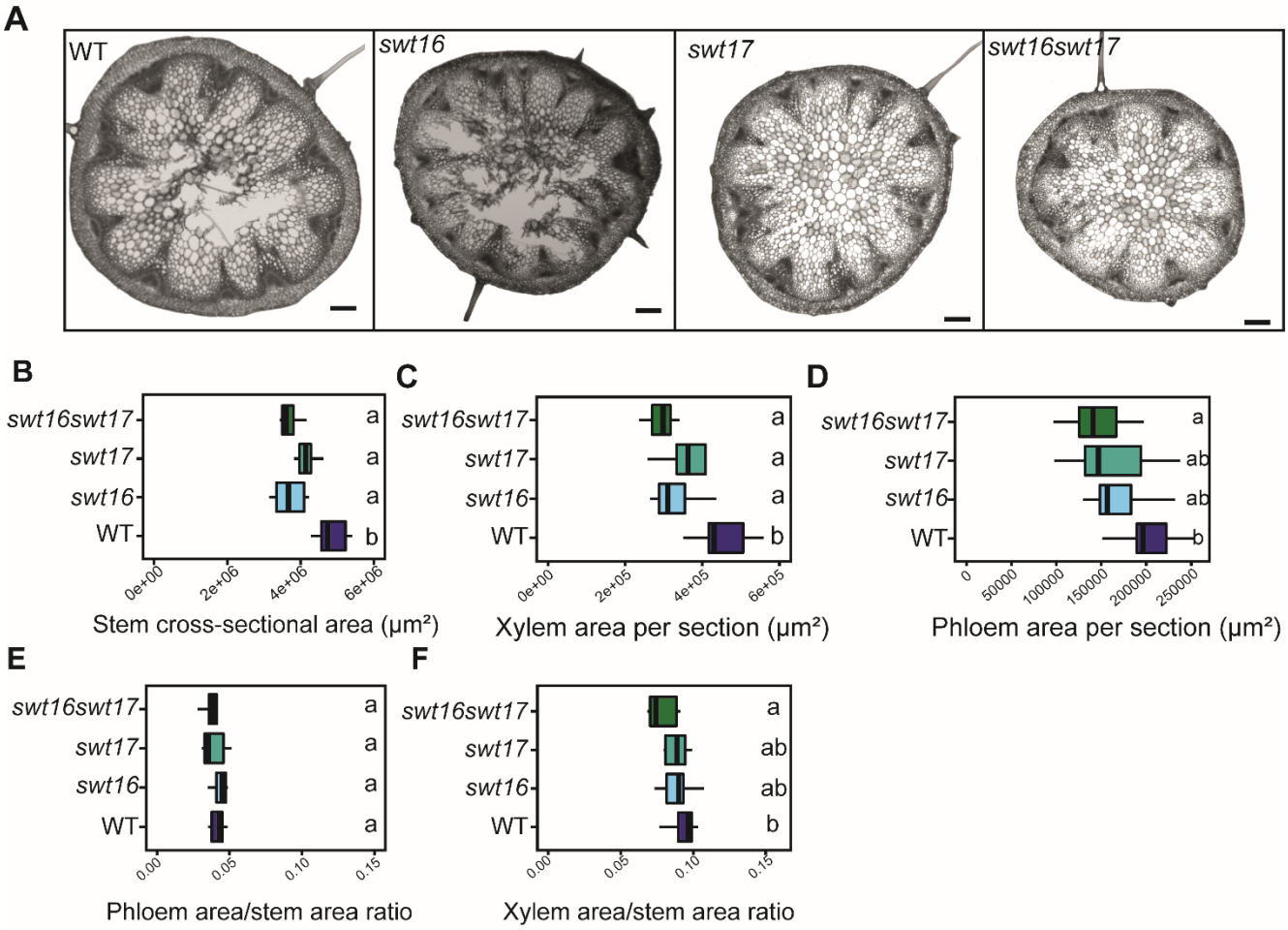

Figure 1. Altered development of the inflorescence stem in the *swt16swt17* double mutant.

(A) Transverse sections of the basal part of the inflorescence stem of 7-week-old plants stained with FASGA solution. Bars = 200 µm.

(B-F) Boxplots showing the inflorescence stem cross-sectional area (B), the area occupied by xylem tissue (C) or phloem tissue (D) within a stem section, the ratio of xylem area to stem area (E) and the ratio of phloem area to stem area (F).

The box and whisker plots represent values from 7 to 8 independent plants. The lines represent median values, the tops and bottoms of the boxes represent the first and third quartiles respectively, and whisker extremities represent maximum and minimum data points. A one-way analysis of variance combined with the Tukey's comparison post-hoc test were performed. Values marked with the same letter were not significantly different from each other, whereas different letters indicate significant differences ($P < 0.05$).

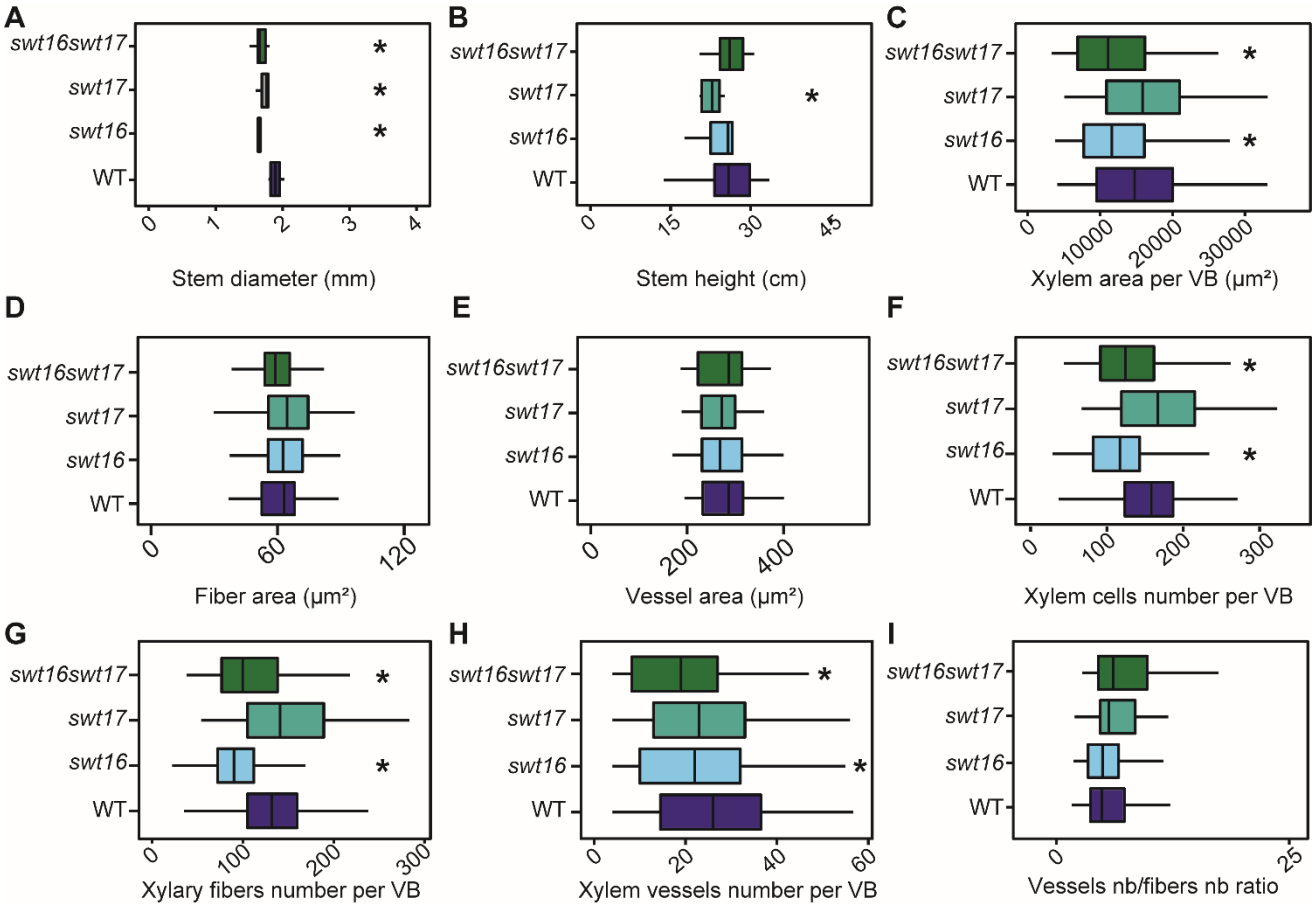

Figure 2. Knockout of *SWEET16* gene expression impacts the proliferation of xylem cells.

(A to I) Boxplots showing the inflorescence stem height (A) and diameter (B), the ratio of vessel number to fiber number (C), the cross-sectional area occupied by xylem tissue per vascular bundle (D), the average cross-sectional area of a xylary fiber (E) or of a xylem vessel (F), and the average number of xylem cells (G), of xylary fiber vessels (H) and of xylem vessels (I) per vascular bundle.

The box and whisker plots represent values from 5 to 7 independent plants (A and B) or from 71, 53, 41 and 50 individual vascular bundles from wild type, *swt16*, *swt17* and *swt16swt17* respectively taken from 5-7 independent plants for each genotype (C-I). The lines represent median values, the tops and bottoms of the boxes represent the first and third quartiles respectively, and whisker extremities represent maximum and minimum data points. Stars denote significant differences between the mutant lines compared to the wild type according to a Student's *t*-test (* $P<0.05$).

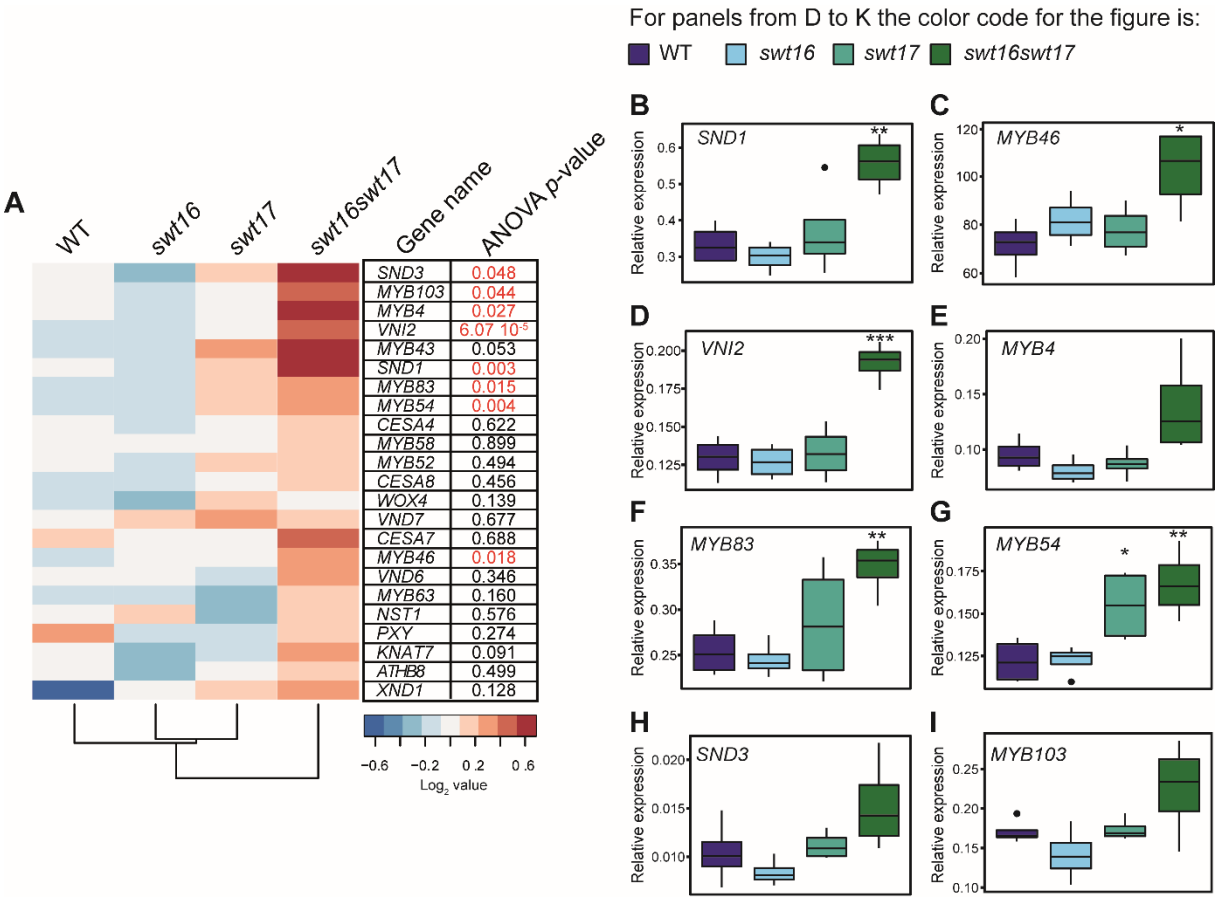

Figure 3. Genes involved in the development of xylem secondary cell wall are deregulated in the *swt16swt17* double mutant.

(A to I) The mRNAs were extracted from total inflorescence stems collected from 7-week-old wild-type, *swt16*, *swt17* and *swt16swt17* plants. The mRNA contents are expressed relative to those of the reference gene *UBQ5*.

(A) Heatmap of expression of candidate genes involved in xylem development and secondary cell wall biosynthesis in the inflorescence stem of the wild type, *swt16*, *swt17* and *swt16swt17* mutants. The values used to build the heatmap are the mean accumulation of transcripts (n=4) normalized by the median value of each gene and expressed as $\log_2$ values. For each gene, the result of one-way ANOVA is displayed beside the heatmap. Those p-values below the significance threshold (P<0.05) are in red.

(B to I) Boxplots showing the relative expression of *SND1* (B), *MYB46* (C), *VNI2* (D), *MYB4* (E), *MYB83* (F), *MYB54* (G), *SND3* (H) and *MYB103* (I). The box-and-whisker plots represent values from 4 biological replicates. The lines represent median values, the tops and bottoms of the boxes represent the first and third quartiles respectively, and the ends of the whiskers

represent maximum and minimum data points. Black dots are outliers. Stars denote significant differences between the mutant line compared to the wild type according to a Student's *t*-test (* $P<0.05$; ** $P<0.01$; *** $P<0.001$). The experiment was repeated twice and gave similar results.

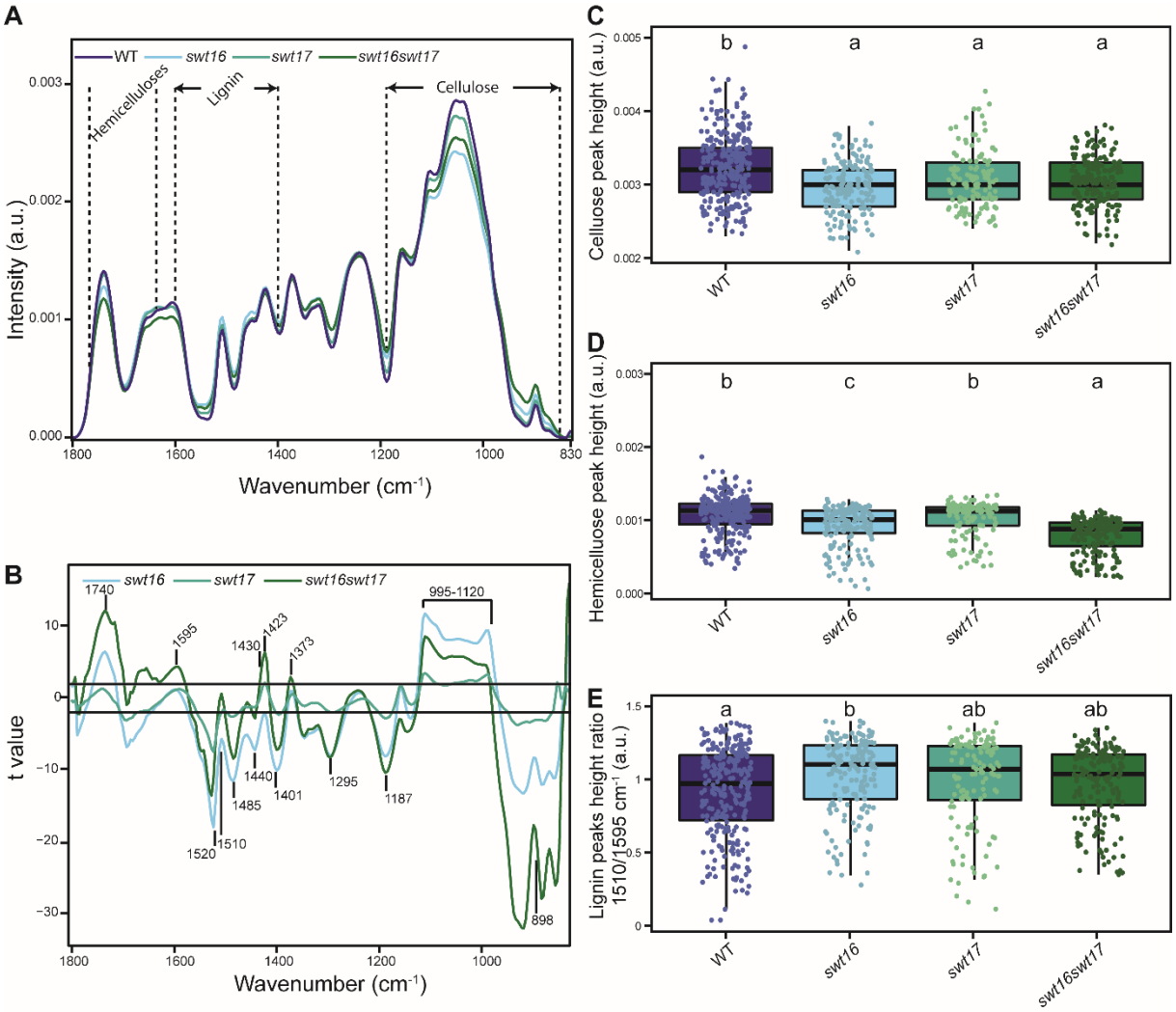

Figure 4. The composition of the xylem secondary cell wall is altered in the *swt16swt17* double mutant.

FTIR spectra were acquired on xylem tissue from sections of the basal part of the inflorescence stem. All spectra were baseline-corrected and area-normalized in the range 1800-800 cm^{-1}.

(A) Average FTIR spectra were generated from 266, 170, 123 and 170 spectra for the wild type, *swt16*, *swt17* and *swt16swt17* respectively, obtained using three independent plants for each genotype.

(B) Comparison of FTIR spectra obtained from xylem cells of the *swt16*, *swt17*, and *swt16swt17* mutants. A Student's *t*-test was performed to compare the absorbances for the wild type, single and double mutants. The results were plotted against the corresponding wavenumbers. T-values (vertical axis) between -2 and +2 correspond to non-significant differences (p-value < 0.05) between the genotypes tested (n=3). T-values above +2 or below -2 correspond to, respectively, significantly weaker or stronger absorbances in the mutant spectra relative to the wild type.

(C to E) Boxplots of the cellulose (C-O vibration band at 1050 cm^{-1}) (C), hemicellulose (C-O and C-C bond stretching at 1740 cm^{-1}) (D) peak height and lignin peak height ratio (1510/1595 cm^{-1}) (E). The lines represent median values, the tops and bottoms of the boxes represent the first and third quartiles respectively, and the ends of the whiskers represent maximum and minimum data points. The boxplots represent values (shown as colored dots) from 266, 170, 123 and 170 spectra from the wild type, *swt16*, *swt17* and *swt16swt17* respectively, obtained from three independent plants for each genotype. A one-way analysis of variance combined with the Tukey's comparison post-hoc test were performed. Values marked with the same letter were not significantly different from each other, whereas different letters indicate significant differences ($P < 0.05$).

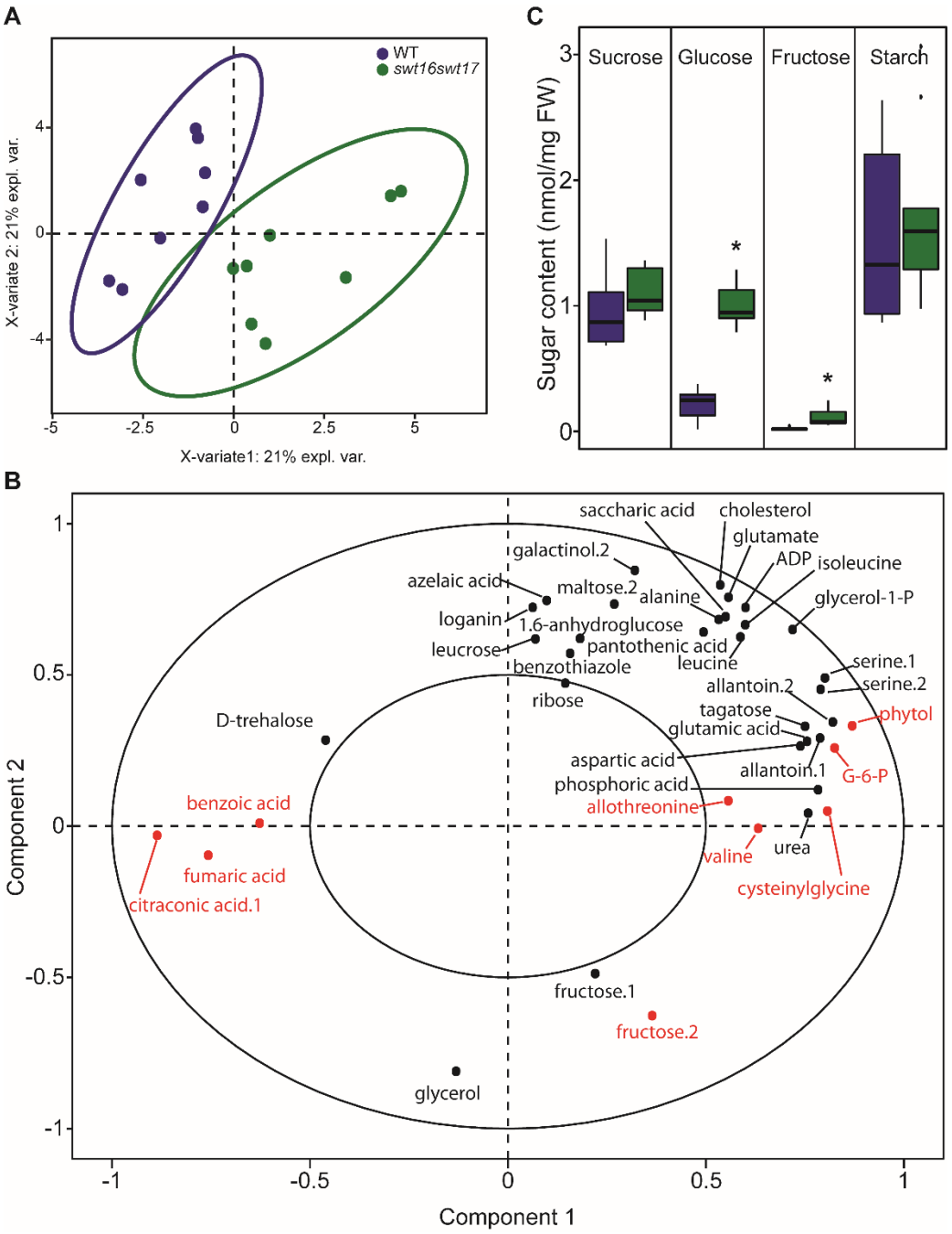

Figure 5. Hexoses accumulate in the inflorescence stem of the *swt16swt17* double mutant.

(A and B) Multivariate analysis of the metabolomic datasets obtained from wild-type and *swt16swt17* inflorescence stems. Metabolites were extracted from eight individual plants for each genotype and analyzed by GC-MS. Plants were grown under long-day conditions for seven weeks. (A) sPLS-DA score plot for wild-type (purple) and *swt16swt17* (green) samples. The variable plot of the sPLS-DA is presented in (B) and metabolites in red are significantly different between the wild type and the *swt16swt17* mutant according to Student's *t*-test ($P<0.05$) (Supplemental Table 3). ADP: adenosine-5-diphosphate; G-6-P: glucose-6-phosphate.

(C) Boxplots showing the sucrose, glucose, fructose and starch contents in the inflorescence stems of the wild type (in purple) and the *swt16swt17* (in green) mutant grown under long-day conditions for seven weeks. The box-and-whisker plots represent values from 9 biological replicates coming from plants grown at two separated times. The lines represent median values, the tops and bottoms of the boxes represent the first and third quartiles respectively, and the ends of the whiskers represent maximum and minimum data points. Black dots are outliers. Asterisks above the boxes indicate statistical differences between genotypes according to Student's *t*-test ($P<0.05$).

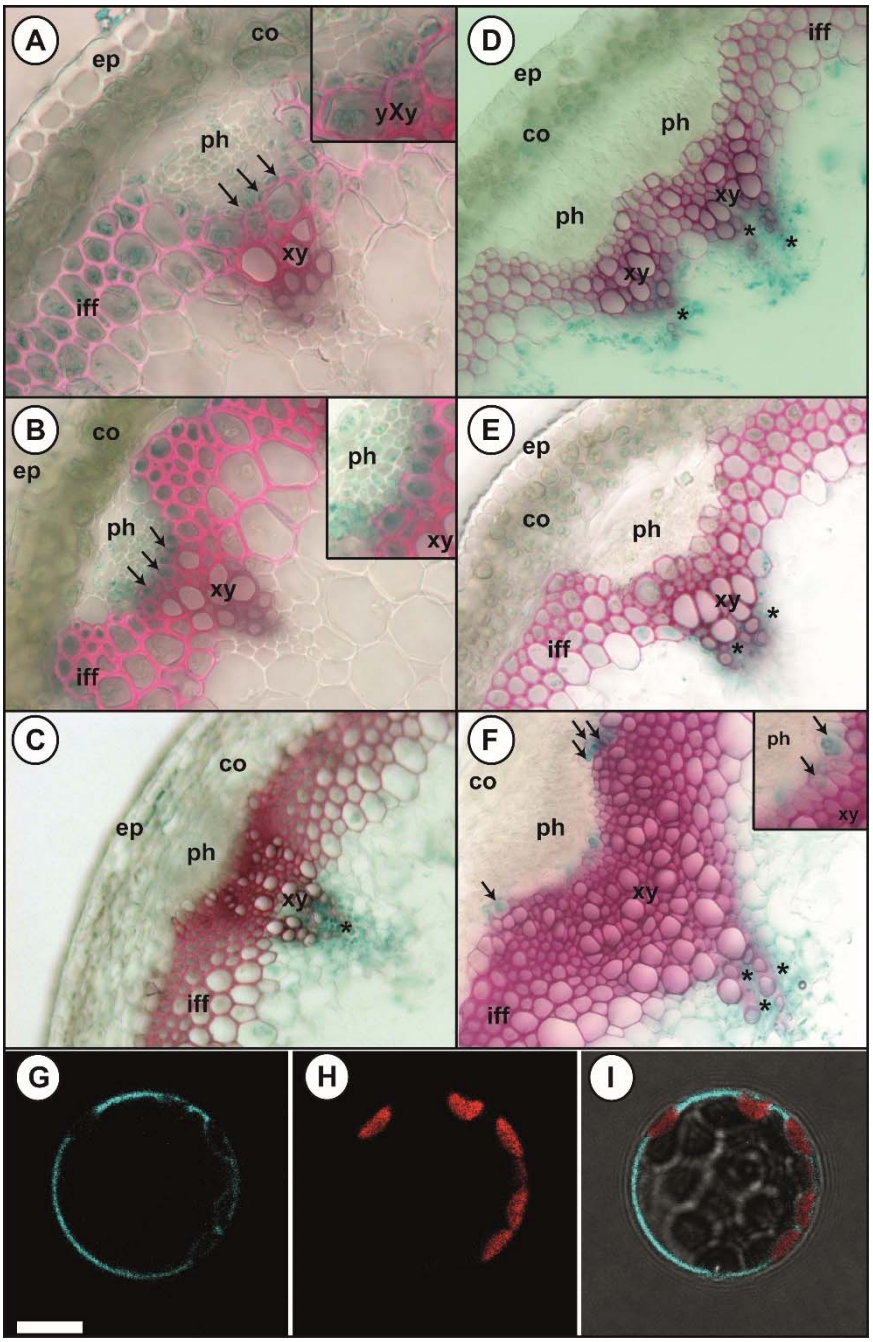

Figure 6. *SWEET16* and *SWEET17* expression patterns vary during inflorescence stem development and the two proteins interact physically.

(A to C) *pSWEET16:GUS* expression pattern in sections taken at different positions in the inflorescence stem of 8-week-old plants. (D to F) *pSWEET17:GUS* expression pattern in sections taken at different positions in the inflorescence stem section of 8-week-old plants. Sections were taken in a stem region where the growth was still rapid (A, D and inset), in a stem region where elongation growth had finished but where thickening of the secondary cell wall was still ongoing (B, E and inset), and at the bottom of the stem, a region that corresponds

to a mature stem (C, F and inset). Arrows point to cells showing blue GUS staining and asterisks indicate xylary parenchyma cells. Lignin is colored pink after phloroglucinol staining. The intensity of the pink color is correlated with the stage of lignification of the xylary vessels. ep: epidermis; co: cortex; iff: interfascicular fibers; ph: phloem; xy: xylem.

(G to I) Fluorescence in an Arabidopsis mesophyll protoplast expressing *SWEET16:cCFP-C* and *SWEET17:nCerulean-C* revealed by false color cyan (G). Chloroplast auto-fluorescence is in false color red (H). Merge of (G) and (H) and bright field image (I). Invaginations around the chloroplasts in (G) and (I) indicate that SWEET16 and SWEET17 interact at the vacuolar membrane. Scale bar = 17 µm.

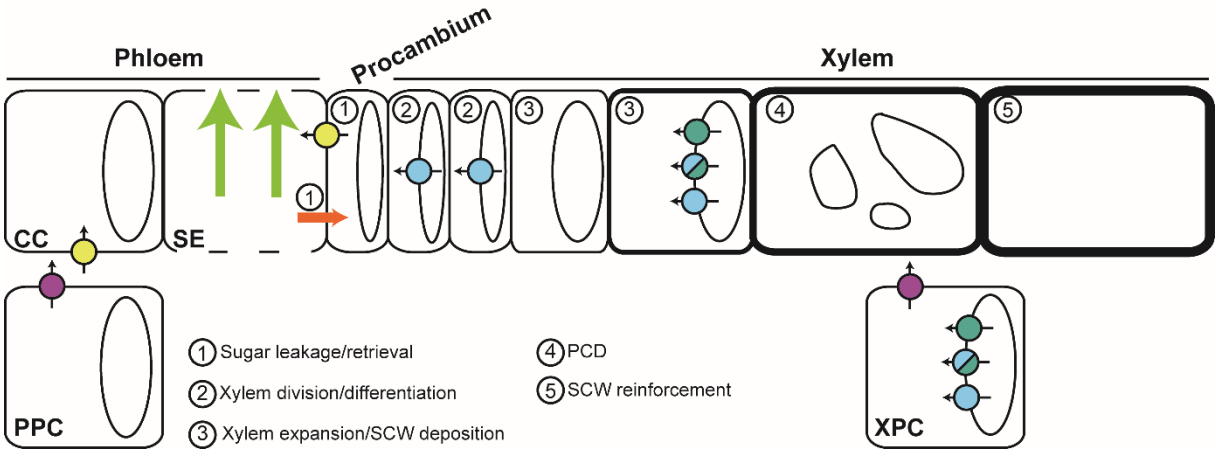

Figure 7. Model for the role of SWEET transporters during xylem development in Arabidopsis inflorescence stems.

This model is based on the results presented in this work on SWEET16 and SWEET17 and those previously published on SWEET11, SWEET12 and SUC2 transporters (Truernit and Sauer, 1995; Chen et al., 2012; Gould et al., 2012; Le Hir et al., 2015). In the phloem tissue, sucrose and hexoses present in the phloem parenchyma cells (PPC) are exported into the apoplastic space between PPC and companion cells (CC) by the sugar transporters SWEET11 and SWEET12 (fuchsia circles). Apoplastic sucrose is then imported into the CC cytosol *via* the SUC2 transporter (yellow circles) before entering the phloem sieve tubes (SE) and being transported over long distances (light green arrows). A part of these sugars leaks from the SE, most probably through plasmodesmata (orange arrow), and reaches axial sinks (e.g. procambium and xylem) while another part of the sugars is reimported inside the SE, mostly through the action of SUC2 (1). In the cells at the cambium-xylem boundary, soluble sugars are probably exported by SWEET16 (light blue circles) into the cytosol in order to sustain the division of xylem cells (2). Given the high cytosolic sugar demand required to sustain the secondary cell wall (SCW) deposition process (3), sugars stored in the vacuole are likely exported into the cytosol through the action of SWEET16 (purple circles) and/or SWEET17 (green circles). Interaction between SWEET16 and SWEET17 is shown as bicolor circles. After the completion of programmed cell death (PCD) and the disintegration of the vacuole (4), the SCW is still being reinforced (5) and we can assume that the sugar demand is still high. At this stage, the sugars stored in the vacuole of the xylary parenchyma cells (XPC) are likely released by SWEET16 and/or SWEET17 and then exported into the apoplastic space by SWEET11 and SWEET12. Whether it is the sugars themselves or more complex cell wall sugar-derived molecules that reach the dead xylem cells remains an open question.

Supplemental Information for

Hexose fluxes, mediated by vacuolar SWEET transporters, are important for xylem development in the inflorescence stem of *Arabidopsis thaliana*.

Emilie Aubry, Beate Hoffmann, Françoise Vilaine, Françoise Gilard, Patrick A.W. Klemens, Florence Guérard, Bertrand Gakière, H. Ekkehard Neuhaus, Catherine Bellini, Sylvie Dinant and Rozenn Le Hir

Corresponding author:

Email: rozenn.le-hir@inrae.fr

This PDF includes:

Supplemental Figures 1 to 5

Supplemental Tables 1 to 5

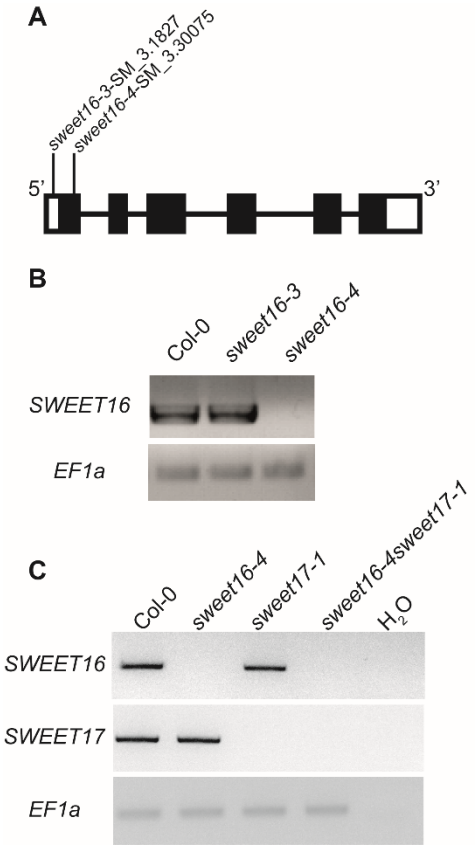

Supplemental Figure 1. Identification of *SWEET16* insertion lines and characterization of the *sweet16-4sweet17-1* mutant.

(A) Positions of the T-DNA insertions in *SWEET16*. White boxes represent the UTR sequences, black boxes are exon sequences and black lines between the black boxes are intron sequences.

(B) RT-PCR analysis of *SWEET16* expression in the single mutant lines *sweet16-3* and *sweet16-4*. Total RNA was isolated from 10-day-old seedlings grown *in vitro* and the resulting cDNAs were used for amplification with primers designed to lie between the start and stop codon of the *SWEET16* sequence (for primer sequences see Supplemental Table 4). Level of expression of EF1α was used as a loading control.

(C) RT-PCR analysis of *SWEET16* and *SWEET17* expression in the floral stem of the *sweet16-4sweet17-1* mutant line. Total RNA was isolated from 7-week-old floral stem of plants grown in long-day conditions. After reverse transcription, the cDNAs were used for amplification with primers designed between the start and stop codon of the *SWEET16* and/or *SWEET17* sequences (for primers sequences see Supplemental Table 4). Expression of EF1α was used as a loading control.

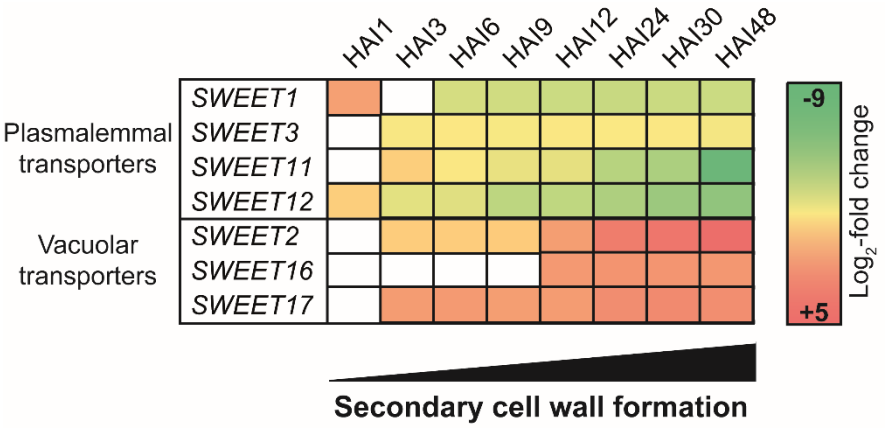

Supplemental Figure 2. Differential expression of *SWEET* genes during secondary cell wall formation in the xylem vessels.

Changes in transcript levels were extracted from data on RNA-seq analysis performed by Li et al. (2016) and presented as log_2-fold changes in comparison with the control (DMSO treatment of the DEX-inducible VND7 line) in colored boxes. HAI1-48 refer to the numbers of Hours After DEX Induction. A white square indicates that the gene was not differentially expressed at that time point.

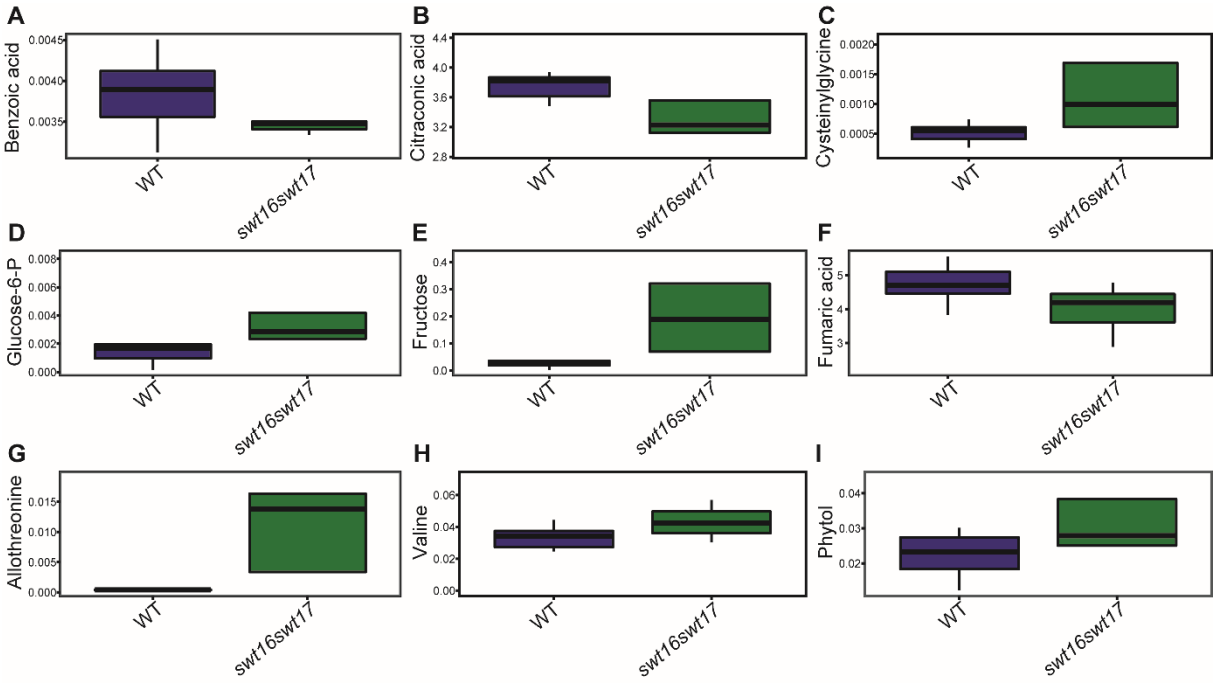

Supplemental Figure 3. Nine out of 158 metabolites identified by GC-MS differ significantly between the wild type and the *swt16swt17* double mutant.

Boxplots showing the relative quantities of benzoic acid (A), citraconic acid (B), cysteinylglycine (C), glucose-6-phosphate (D), fructose (E), fumaric acid (F), allothreonine (G), valine (H) and phytol (I) in the inflorescence stem of the wild type and the *swt16swt17* mutant grown in long-day conditions for seven weeks. Each of the box-and-whisker plots represents values from 8 individual plants for each genotype. The lines represent median values, the tops and bottoms of the boxes represent the first and third quartiles respectively, and the ends of the whiskers represent maximum and minimum data points.

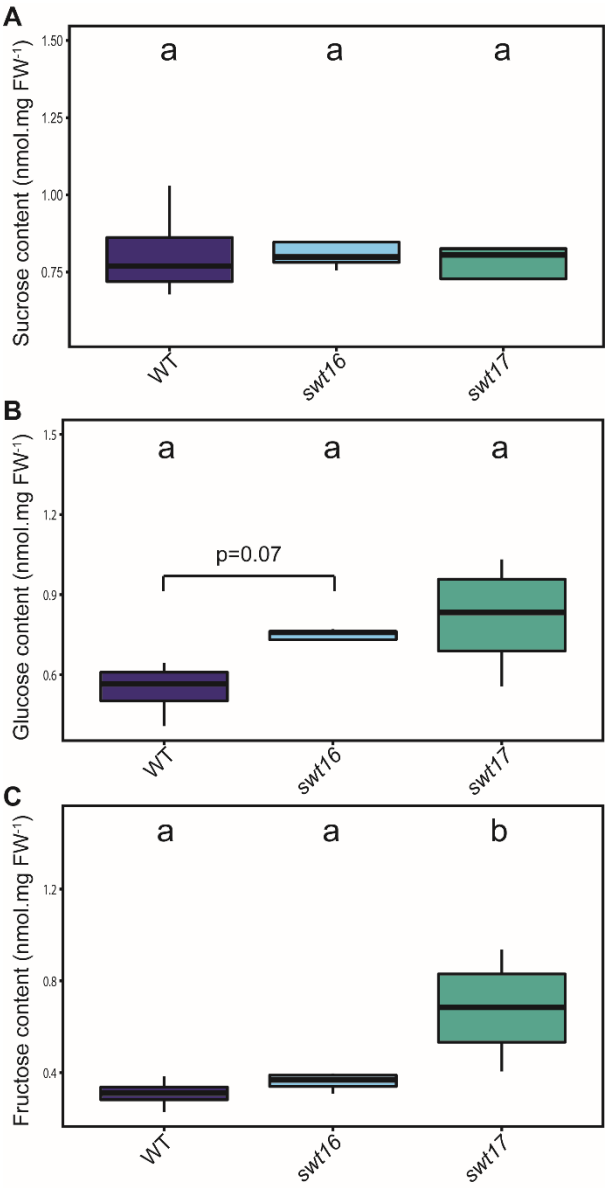

Supplemental Figure 4. Fructose accumulation in the inflorescence stem of the *swt17* mutant.

(A-C) Boxplots showing the sucrose (A), glucose (B) and fructose (C) contents of the inflorescence stems of the wild type and the *swt16* and *swt17* mutants grown under long-day conditions for seven weeks. Each of the box-and-whisker plots represents values from 4 biological replicates for each genotype. The lines represent median values, the tops and bottoms of the boxes represent the first and third quartiles respectively and the ends of the whiskers represent maximum and minimum data points. A one-way analysis of variance combined with the Tukey's comparison post-hoc test was performed. Values marked with the same letter were not significantly different from each other, whereas different letters indicate significant differences ($P < 0.05$).

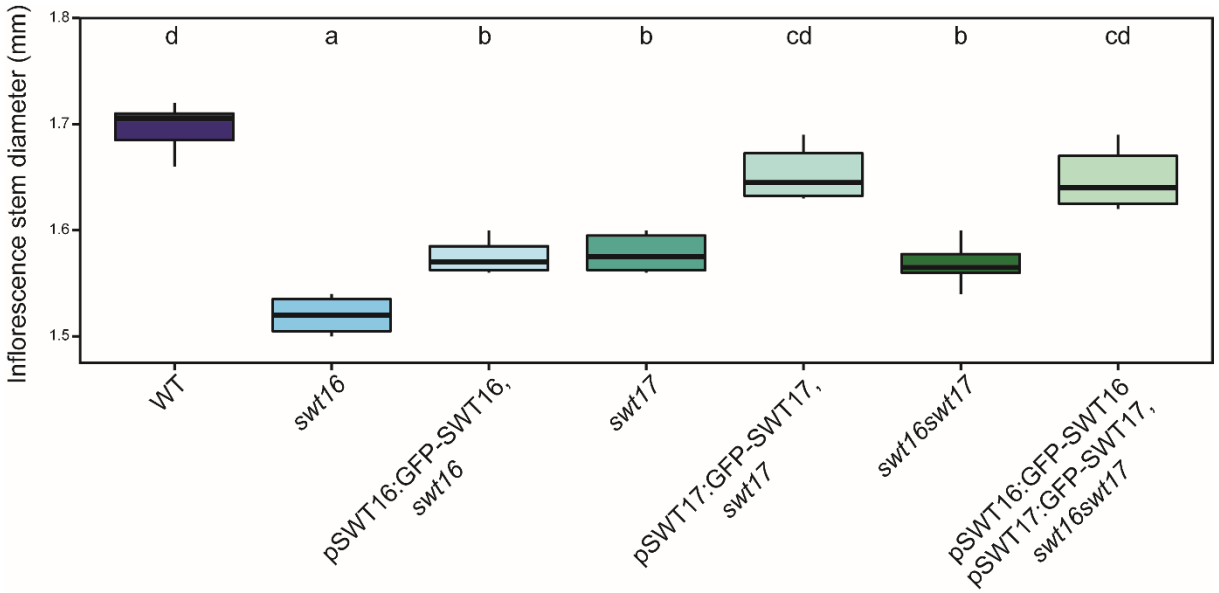

Supplemental Figure 5. Checking the functionality of the translational GFP fusions by complementation of the inflorescence stem phenotype of the single and double mutants.

The diameter was measured with a digital caliper at the bottom of the main inflorescence stem on plants grown for 7 weeks in long-day conditions. The lines represent median values, the tops and bottoms of the boxes represent the first and third quartiles respectively, and the ends of the whiskers represent maximum and minimum data points. Values represent means from six biological replicates. A one-way analysis of variance combined with the Tukey's comparison post-hoc test were performed. Values marked with the same letter were not significantly different from each other, whereas different letters indicate significant differences ($P < 0.05$).

Supplemental Table 1. *p* values from pairwise comparisons (Tukey post-hoc test) between genotypes for anatomical parameters measured in the xylem tissue of the inflorescence stem. Values in grey boxes are significantly different at the 95% confidence level.

Genotypes compared	Stem height	Stem diameter	Total xylem area	Fiber area	Vessel area	Total xylem number	Fiber number	Vessel number	Ratio vessels/fibers
WT - *s11*	0.999	0.012	0.001	0.686	0.882	<0.001	0.002	0.001	0.887
WT - *s12*	0.999	0.681	0.302	0.999	0.999	0.620	0.853	0.119	0.887
WT - *s11s12*	0.556	<0.001	<0.001	1	0.815	<0.001	<0.001	<0.001	0.766
WT - *s16*	1	0.04	0.05	0.864	0.994	<0.001	<0.001	0.350	1
WT - *s17*	0.930	0.055	0.999	0.538	0.875	0.909	0.786	0.999	0.998
WT - *s16s17*	0.999	0.002	0.036	1	0.999	0.031	0.074	0.026	0.904
WT - *qua*	0.068	<0.001	<0.001	0.815	0.930	<0.001	<0.001	<0.001	0.999
s11 - s12	0.999	0.576	0.668	0.582	0.989	0.294	0.267	0.889	1
s11 - s16	0.999	0.999	0.926	0.999	0.999	0.999	0.999	0.539	0.926
s11 - s17	0.997	0.996	0.001	0.999	1	<0.001	<0.001	0.015	0.998
s12 - s16	0.999	0.407	0.999	0.769	0.999	0.349	0.119	0.999	0.929
s12 - s17	0.916	0.910	0.191	0.446	0.988	0.112	0.143	0.360	0.999
s11s12 - s11	0.870	<0.001	0.842	0.771	1	0.511	0.349	0.999	0.999
s11s12 - s12	0.559	<0.001	0.027	0.999	0.978	<0.001	<0.001	0.713	0.999
s11s12 - s16	0.628	<0.001	0.104	0.913	0.997	0.277	0.389	0.306	0.838
s11s12 - s17	0.994	<0.001	<0.001	0.645	1	<0.001	<0.001	0.004	0.992
s11s112 - s16s17	0.512	<0.001	0.163	1	0.981	0.027	0.013	0.909	0.999
s11s12 - qua	0.974	0.999	0.998	0.891	0.999	0.999	0.998	0.999	0.737
s16s17 - s11	0.999	0.999	0.965	0.746	0.991	0.941	0.952	0.982	0.999
s16s17 - s12	1	0.316	0.996	0.999	1	0.923	0.890	0.999	1
s16s17 - s16	0.999	0.999	0.999	0.899	0.999	0.976	0.852	0.970	0.941
s16s17 - s17	0.899	0.951	0.025	0.614	0.990	0.002	0.002	0.143	0.999
s16s17 - qua	0.064	<0.001	0.029	0.878	0.997	0.003	0.001	0.795	0.876
qua - s11	0.270	<0.001	0.468	0.082	0.999	0.188	0.095	0.999	0.856
qua - s12	0.087	<0.001	0.003	0.968	0.996	<0.001	<0.001	0.544	0.858
qua - s16	0.098	<0.001	0.015	0.142	0.999	0.067	0.102	0.178	0.999
qua - s17	0.613	<0.001	<0.001	0.047	0.999	0	0	0.001	0.994

Supplemental Table 2. Genes co-regulated during secondary cell wall formation.

Genes related to secondary cell wall formation and sugar transport were selected from differentially expressed genes associated with Cluster 21, as identified in Supplemental Table S7 in Li et al. (2016).

AGI	Name	Biological process
AT1G43790	TED6	Cellulose biosynthesis/assembly
AT3G16920	CTL2	Cellulose biosynthesis/assembly
AT4G18780	CesA8	Cellulose biosynthesis/assembly
AT5G03170	AtFLA11	Cellulose biosynthesis/assembly
AT5G17420	CesA7	Cellulose biosynthesis/assembly
AT5G44030	CesA4	Cellulose biosynthesis/assembly
AT1G28470	SND3	Transcriptional regulation
AT1G62990	IRX11	Transcriptional regulation
AT1G63910	MYB103	Transcriptional regulation
AT1G66230	MYB20	Transcriptional regulation
AT2G45420	LBD18	Transcriptional regulation
AT4G00220	LBD30	Transcriptional regulation
AT4G12350	MYB42	Transcriptional regulation
AT4G22680	MYB85	Transcriptional regulation
AT4G28500	SND2	Transcriptional regulation
AT5G12870	MYB46	Transcriptional regulation
AT1G19300	PARVUS	Xylan biosynthesis
AT1G27440	IRX10/GUT2	Xylan biosynthesis
AT2G28110	FRA8	Xylan biosynthesis
AT2G37090	IRX9	Xylan biosynthesis
AT3G18660	GUX1	Xylan biosynthesis
AT3G50220	IRX15	Xylan biosynthesis
AT4G33330	GUX2	Xylan biosynthesis
AT5G46340	RWA1	Xylan biosynthesis
AT5G54690	IRX8	Xylan biosynthesis
AT5G67210	IRX15L	Xylan biosynthesis
AT4G15920	SWEET17	Fructose transport
AT3G14770	SWEET2	Glucose transport
AT1G08920	ESL1	Hexose transport
AT1G11260	STP1	Hexose/H+ co-transport
AT5G26340	STP13	Hexose/H+ co-transport
AT2G20780	PMT4	Polyol/monosaccharide transport

Supplemental Table 3. *p* values from *t*-test of metabolites identified from GC-MS analysis. Values in red boxes are significantly different at the 95% confidence level. Metabolites are organized in classes according to the Golm metabolome database (http://gmd.mpimp-golm.mpg.de/Metabolites/List.aspx).

Metabolite	*p* value	Class
aspartic acid 1	0.410	Acid (Amino)
aspartic acid 2	0.101	Acid (Amino)
Beta- alanine 1	0.678	Acid (Amino)
DL-3-aminoisobutyric acid 2	0.893	Acid (Amino)
DL-isoleucine 1	0.580	Acid (Amino)
DL-isoleucine 2	0.345	Acid (Amino)
gamma-aminobutyric acid (GABA)	0.344	Acid (Amino)
glycine	0.550	Acid (Amino)
L-alanine 2	0.553	Acid (Amino)
L-allothreonine 2	0.047	Acid (Amino)
L-asparagine 2	0.115	Acid (Amino)
L-glutamic acid 2	0.066	Acid (Amino)
L-glutamic acid 3 (dehydrated)	0.602	Acid (Amino)
L-glutamine 1	0.941	Acid (Amino)
L-glutamine 2	0.224	Acid (Amino)
L-glutamine 3	0.106	Acid (Amino)
L-leucine 2	0.547	Acid (Amino)
L-lysine 2	0.372	Acid (Amino)
L-ornithine 2	0.178	Acid (Amino)
L-proline 2	0.283	Acid (Amino)
L-serine 1	0.096	Acid (Amino)
L-serine 2	0.066	Acid (Amino)
L-threonine 1	0.415	Acid (Amino)
L-threonine 2	0.232	Acid (Amino)
L-tryptophan 2	0.497	Acid (Amino)
L-valine 2	0.047	Acid (Amino)
norvaline 1 (pmm)	0.973	Acid (Amino)
Phenylalanine 1	0.162	Acid (Amino)
Phenylalanine 1	0.124	Acid (Amino)
tyrosine 2	0.319	Acid (Amino)
citrulline 2	0.200	Acid (Amino). non proteinogen
acetyl-L-serine 1	0.153	Acid (Amino. N-acyl-)

Metabolite	*p* value	Class
4-hydroxybenzoic acid	0.634	Acid (Aromatic)
benzoic acid (pmm)	0.027	Acid (Aromatic)
mandelic acid	0.552	Acid (Aromatic)
salicylic acid	0.955	Acid (Aromatic)
glycolic acid (sl)	0.931	Acid (carboxy)
glyoxylic acid	0.736	Acid (carboxy)
adipic acid	0.222	Acid (Dicarboxylic)
azelaic acid	0.352	Acid (Dicarboxylic)
citraconic acid 1	0.008	Acid (Dicarboxylic)
citraconic acid 3	0.857	Acid (Dicarboxylic)
citraconic acid 5	0.763	Acid (Dicarboxylic)
fumaric acid	0.039	Acid (Dicarboxylic)
glutaconic acid 1	0.158	Acid (dicarboxylic)
glutaric acid (pmm)	0.662	Acid (Dicarboxylic)
itaconic acid	0.114	Acid (Dicarboxylic)
maleic acid	0.556	Acid (Dicarboxylic)
malonic acid 1	0.143	Acid (Dicarboxylic)
oxalic acid	0.668	Acid (Dicarboxylic)
succinic acid	0.548	Acid (Dicarboxylic)
arachidic acid	0.779	Acid (Fatty acid trimethylsilyl ester)
capric acid	0.698	Acid (Fatty acid trimethylsilyl ester)
elaidic acid	0.787	Acid (Fatty acid trimethylsilyl ester)
lauric acid	0.505	Acid (Fatty acid trimethylsilyl ester)

Metabolite	*p* value	Class
linoleic acid	0.711	Acid (Fatty acid trimethylsilyl ester)
myristic acid	0.253	Acid (Fatty acid trimethylsilyl ester)
Myristic Acid d27	0.387	Acid (Fatty acid trimethylsilyl ester)
oleic acid	0.956	Acid (Fatty acid trimethylsilyl ester)
palmitic acid	0.609	Acid (Fatty acid trimethylsilyl ester)
palmitoleic acid	0.544	Acid (Fatty acid trimethylsilyl ester)
stearic acid	0.569	Acid (Fatty acid trimethylsilyl ester)
hexanoic acid (sl)	0.277	Acid (Fatty acid)
D-saccharic acid	0.625	Acid (Hexaric)
galactonic acid 2	0.717	Acid (Hexonic)
gluconic acid 2	0.669	Acid (Hexonic)
gluconic acid lactone 1	0.249	Acid (Hexonic. lactone)
galacturonic acid 1	0.302	Acid (Hexuronic)
citramalic acid	0.460	Acid (hydroxy ducarboxy)
dehydroascorbic acid 1	0.525	Acid (Hydroxy)
dehydroascorbic acid 4	0.728	Acid (Hydroxy)
D-malic acid	0.795	Acid (Hydroxy)
glyceric acid	0.731	Acid (Hydroxy)
L-(+) lactic acid (sl)	0.562	Acid (Hydroxy)
L-ascorbic acid	0.162	Acid (Hydroxy)
pantothenic acid 2	0.784	Acid (Hydroxy)
quinic acid	0.195	Acid (Hydroxy)
shikimic acid	0.744	Acid (Hydroxy)
tagatose 1	0.051	Acid (Hydroxy)
threonic acid	0.535	Acid (Hydroxy)
erythrono-1.4-lactone	0.915	Acid (Hydroxy. lactone)
alpha ketoglutaric acid	0.114	acid (Keto)
nicotinic acid	0.308	Acid (N-heterocycle)
B28pyruvic acid (sl)	0.940	Acid (Oxo)
3.5-dimethoxy-4-hydroxycinnamique	0.322	Acid (Phenylpropanoic)

Metabolite	*p* value	Class
cinnamic acid	0.847	Acid (Phenylpropanoic)
ferulic acid	0.943	Acid (Phenylpropanoic)
phosphoric acid	0.059	Acid (Phosphate)
citric acid	0.421	Acid (Tricarboxylic)
isocitric acid	0.343	Acid (Tricarboxylic)
trans-aconitic acid	0.282	Acid (Tricarboxylic)
1-decanol (decyl alcohol)	0.114	**Alcohol**
1-nonanol	0.490	**Alcohol**
ethanolamine	0.741	Alcohol (Amino)
triethanolamine	0.560	Alcohol (Amino)
phytol 2	0.041	Alcohol (Isoprenoid)
beta-glycerolphosphate	0.540	Alcohol (Phosphate)
glycerol 1-phosphate	0.305	Alcohol (Phosphate)
urea	0.093	Amide
allantoin 1	0.100	Amide (N-heterocycle)
allantoin 3	0.078	Amide (N-heterocycle)
putrescine	0.891	Amine (Poly)
galactinol 2	0.656	Conjugate (Hexosyl. Inositol)
galactitol	0.910	Conjugate (Hexosyl. Inositol)
2.3-butanediol 2	0.157	misc
2-hydroxypyridine	0.942	misc
3-(methylthio)-propylamine	0.449	misc
3-indoleacetonitrile	0.225	misc
4-hydroxypyridine	0.369	misc
acetohydroxamic acid	0.930	misc
benzothiazole	0.496	misc
cyclohexanamine	0.890	misc
cysteinylglycine 1	0.040	misc
homovanillic acid (HVA)	0.839	misc
isopropyl beta-D-1-thiogalacto	0.728	misc
loganin	0.357	misc
neohesperidin	0.222	misc
N-ethylglycine 2	0.824	misc
N-methylalanine	0.317	misc

Metabolite	*p* value	Class
O-phosphocolamine	0.158	misc
porphine 1	0.736	misc
tyramine	0.691	misc
adenosine 5'-diphosphate	0.589	Nucleoside
D-sorbitol	0.539	Polyol (Hexitol)
myo-inositol	0.171	Polyol (Inositol)
glycerol	0.444	Polyol (Triol)
adenine 1	0.357	Purine
uric acid 1	0.711	Purine
9H-purine-6-amine	0.133	purine (cytokinine)
beta-gentiobiose 2	0.481	Sugar (Disaccharide)
lactose 1	0.461	Sugar (Disaccharide)
leucrose	0.386	Sugar (Disaccharide)
maltose 2	0.716	Sugar (Disaccharide)
melibiose 1	0.846	Sugar (Disaccharide)
Sucrose	0.995	Sugar (Disaccharide)
fructose 1	0.071	Sugar (Hexose)
fructose 2	0.009	Sugar (Hexose)
D (+)altrose 1	0.336	Sugar (Hexose. aldose)
D-(+) trehalose	0.073	Sugar (Hexose. aldose)
D-glucose 1	0.200	Sugar (Hexose. aldose)
D-glucose 2	0.325	Sugar (Hexose. aldose)
D-mannose 1	0.383	Sugar (Hexose. aldose)
Glucopyranose	0.285	Sugar (Hexose. aldose)
1.5-anhydro-D-sorbitol	0.303	Sugar (Hexose. aldose. anhydride)
1.6-anhydro-glucose	0.435	Sugar (Hexose. aldose. anhydride)
rhamnose 1	0.339	Sugar (Hexose. deoxy)
rhamnose 2	0.330	Sugar (Hexose. deoxy)
arabinose	0.639	Sugar (Pentose. aldose)
ribose	0.524	Sugar (Pentose. aldose)

Metabolite	*p* value	Class
xylose 2	0.591	Sugar (Pentose. aldose)
xylulose	0.773	Sugar (Pentose. ketose)
D-glucose-6-phosphate 1	0.126	Sugar (Phosphate)
D-glucose-6-phosphate 2	0.040	Sugar (Phosphate)
fructose 6-phosphate	0.104	Sugar (Phosphate)
sedoheptulose 7-phosphate	0.221	Sugar (Phosphate)
Raffinose (pmm)	0.931	Sugar (Trisaccharide)
beta-sitosterol	0.212	Terpenoid (**Sterol**)
cholesterol	0.816	Terpenoid (**Sterol**)

Supplemental Table 4. Primers used for characterizing mutant lines and for cloning purposes

Accession number	Primer name	Sequence (5'→3')	Amplicon size (bp)	Purpose
At3g16690	sweet16-3_LP	TGCAACTATGGAAATGGAAGG	1655	Genotyping
	sweet16-3_RP	GATTCAGCAAGAGCACCAAAG		
	sweet16-4_LP	TGCAAATAATTTAGCAACCGC	1742	
	sweet16-4_RP	TATAAATGATCTGGGGCCATC		
	SWEET16ATG-stopF	ATGGCAGACTTGAGTTTTTATGTC	693	Full-length PCR
	SWEET16ATG-stopR	TTAAGCGAGGAGAGGTTGATTT		
	Bam-pS16-5'	CGGGATCCTGATTACAACATTACAACATTCAGTG	1295	**Cloning** GFP fusions
	Eco1-pS16-3'	CGGAATTCCTCTGAGGATGGGTTTCTGAG		
	Not-S16-5'	ATAAGAATGCGGCCGCATGGCAGACTTGAGTTTTTATG	1863	
	Eco5-S16-3'	ATAAGAATGCGGCCGCCATGGCAGACTTGAGTTTTTATGT		
At4g15920	sweet17-1_LP	TGATGTGAGGCCTTCCTCTT	771	Genotyping
	sweet17-1_RP	CCGTTTTGGTTGTCGTTTTT		
	Sal-pS17-5'	ACGCGTCGACAAAGAGATAAATTAAATGAGATTTGTATGG	2004	**Cloning** GFP fusions
	Kpn-pS17-3'	GGGGTACCTATTGGAGAAAGAGTTTCTGAG		
	NotI-S17-5'	ATAAGAATGCGGCCGCCATGGCAGAGGCAAGTTTCTATATC	2601	
	Eco5-S17-3'	CCCGGATATCTTAAGAGAGGAGAGGTTCAACACG		
eGFP	Eco1-eGFP5'	CGGAATTCATGGTGAGCAAGGGCGAGGA	714	Cloning
	Not-eGFP-3'0stop	ATAAGAATGCGGCCGCCTTGTACAGCTCGTCCATGCC		

Supplemental Table 5. Primers used for quantifying gene expression by qPCR

Accession number	Gene name	Forward sequence (5'→3')	Reverse sequence (5'→3')	Size (bp)	Efficiency	Reference
At5g12870	*MYB46*	GAATGTGAAGAAGGTGATTGGTACA	CGAAGGAACCTCAGTGTTCATCA	150	73.5	(Takeuchi et al., 2018)
At3g08500	*MYB83*	GTCGCCTTCGCTGGATCAAT	AAGCCGCTTCTTCAATGTCG	191	85.8	(Shafi et al., 2019)
At5g61480	*PXY*	TTCAAACCGACGAATCCATGT	TTATCCACTTGTAAAGTGTAAGCATATTCT	85	95.4	(Smetana et al., 2019)
At1g46480	*WOX4*	GACAAGAACATCATCGTCACTAGACA	TTCTCCACCATTGGTTCTCTCA	51	92.4	(Smetana et al., 2019)
At1g32770	*SND1/ NST3*	GCAGCAACTGGGCTAGTCTT	CCCATCGCTGCATCATAGTA	126	93.6	This study
At4g32880	*AtHB8*	AACACCACTTGACCCCTCAACATCAG	CACGCAACCAACAAGGCTTATCC	276	91.9	(Carlsbecker et al., 2010)
At5g44030	*CESA4*	TGCCTATGGATCGGAAAATGGA	ACGTTCTTTCCACTCCGCAT	145	95.4	(Shafi et al., 2019)
At5g17420	*CESA7*	TTGTGTACGTGTCCCGTGAG	ATTTGTGAGTACGCCTGCCA	98	101.1	(Shafi et al., 2019)
At4g18780	*CESA8*	AGGTCTCCCATCTGCAACAC	CTCATCGTAAGGATTGCCGC	168	97.9	(Shafi et al., 2019)
At1g28470	*SND3*	TTCTTCCACCGGCCATCAAA	CTGGCGACCATAGTTGGTGT	183	103.8	(Shafi et al., 2019)
At1g63910	*MYB103*	GGGAAACAGGTGGGCTCATA	TGGTAGAGGCCTCGATGGTA	197	100.3	(Shafi et al., 2019)
At1g62990	*KNAT7*	GAAGCTGTTATGGCTTGCCG	TCGGTAGCAACGGACCAAAT	190	95.3	(Shafi et al., 2019)
At1g79180	*MYB63*	GACAAACCCGATCTGCTGGA	CCCGAGTTCGCTTTCTAGGT	189	99.8	(Shafi et al., 2019)
At1g16490	*MYB58*	AAGCGGGTTCAAAAGGTTCT	GCATCATCGTCTTTGCTTGA	109	98	This study
At5g13180	*VNI2*	CTCCTTTGCCAGCTTCAATC	GGTTAGACCGGTTCCCATTT	138	97.8	This study
At5g64530	*XND1*	CCCGACCTTGATCTTTACCA	CCCAATACCCATTGCTTGTC	124	94.9	This study
At4g39620	*MYB4*	ACAGAGGGATTGATCCAACG	TCGACCTTTGGAGCAGAAGT	133	97.9	This study
At1g17950	*MYB52*	CCGGTCGAACTGATAACGCT	ACCAATCATCCCAGTCGCAG	131	103	(Shafi et al., 2019)
At1g73410	*MYB54*	AACCGAAACCCTTTCACGGA	ACGAGGCTTAGAGGTTTGGC	174	87.8	(Shafi et al., 2019)
At5g16600	*MYB43*	CCATGCGCAACTTGGCAATA	CCCTTGAGCTTGTTGTGAAGC	178	100.1	(Shafi et al., 2019)
At3g62250	*UBQ5*	CCAAGCCGAAGAAGATCAAG	ACTCCTTCCTCAAACGCTGA	105	98.6	This study

SUPPLEMENTAL REFERENCES

Carlsbecker, A., Lee, J. Y., Roberts, C. J., Dettmer, J., Lehesranta, S., Zhou, J., Lindgren, O., Moreno-Risueno, M. A., Vatén, A., Thitamadee, S., et al. (2010). Cell signalling by microRNA165/6 directs gene dose-dependent root cell fate. *Nature* **465**, 316–321.

Chen, L.-Q., Hou, B.-H., Lalonde, S., Takanaga, H., Hartung, M. L., Qu, X.-Q., Guo, W.-J., Kim, J.-G., Underwood, W., Chaudhuri, B., et al. (2010). Sugar transporters for intercellular exchange and nutrition of pathogens. *Nature* **468**, 527–532.

Li, Z., Omranian, N., Neumetzler, L., wang, ting, Herter, T., Usadel, B., Demura, T., Giavalisco, P., Nikoloski, Z. and Persson, S. (2016). A Transcriptional and Metabolic Framework for Secondary Wall Formation in Arabidopsis. *Plant Physiol.* pp.01100.2016.

Poschet, G., Hannich, B., Raab, S., Jungkunz, I., Klemens, P. A. W., Krueger, S., Wic, S., Neuhaus, H. E. and Buttner, M. (2011). A Novel Arabidopsis Vacuolar Glucose Exporter Is Involved in Cellular Sugar Homeostasis and Affects the Composition of Seed Storage Compounds. *Plant Physiol.* **157**, 1664–1676.

Sellami, S., Le Hir, R., Thorpe, M. R., Vilaine, F., Wolff, N., Brini, F. and Dinant, S. (2019). Salinity effects on sugar homeostasis and vascular anatomy in the stem of the *Arabidopsis thaliana* inflorescence. *Int. J. Mol. Sci.* **20**, 3167.

Shafi, A., Gill, T., Zahoor, I., Ahuja, P. S., Sreenivasulu, Y., Kumar, S. and Singh, A. K. (2019). Ectopic expression of SOD and APX genes in Arabidopsis alters metabolic pools and genes related to secondary cell wall cellulose biosynthesis and improve salt tolerance. *Mol. Biol. Rep.* **46**, 1985–2002.

Smetana, O., Mäkilä, R., Lyu, M., Amiryousefi, A., Rodríguez, F. S., Wu, M., Solé-gil, A., Gavarrón, M. L., Siligato, R., Miyashima, S., et al. (2019). High levels of auxin signalling define the stem-cell organizer of the vascular cambium. *Nature* **565**, 485–491.

Takeuchi, M., Watanabe, A., Tamura, M. and Tsutsumi, Y. (2018). The gene expression analysis of Arabidopsis thaliana ABC transporters by real-time PCR for screening monolignol-transporter candidates. *J. Wood Sci.* **64**, 477–484.